energy&fuels

pubs.acs.org/EF Article

Experimental and Simulation Study for the Dissociation Behavior of Gas Hydrates—Part II: sII Mixed Gas Hydrates

Mengdi Pan,*,∞ Parisa Naeiji,∞ and Judith M. Schicks

Cite This: *Energy Fuels* 2023, 37, 4497−4514

Read Online

ACCESS | Metrics & More | Article Recommendations | Supporting Information

ABSTRACT: This study is an extension of our research on the dissociation behavior of sI CH_4 hydrates (Part I). In this study, investigations of the dissociation of binary and multicomponent structure II hydrates were carried out. A novel approach involving *in situ* and *ex situ* Raman spectroscopic measurements together with molecular dynamics simulations were applied for a systematic assessment of the hydrate dissociation and gas release behavior due to the destabilization of hydrate cavities. The hydrate decomposition was induced by thermal stimulation to mimic the warming of oceans and atmosphere brought by climate changes. The interactions between the released gas, aqueous phase, and hydrates were described. The results demonstrated that in the vicinity of the hydrate surface, the liquid phase was oversaturated with the gas molecules and some unstable partial hydrate cavities were also formed. Consequently, the release of gas was temporarily stopped or very slow. Throughout the process, the hydrate underwent decomposition−reformation−continuing decomposition until the crystal disappeared. A faster breakdown of small cavities (5^{12}) was recorded, leading to an increase in the large-to-small cavity ratio during dissociation. Moreover, the results indicated a faster release of CH_4 molecules compared to C_3H_8 over the dissociation process of the sII CH_4−C_3H_8 hydrate. This could be due to the higher diffusivity of CH_4 molecules from the hydrate surface to the gas phase as well as its lower potential to stabilize the cavities compared to C_3H_8. The release of CH_4 molecules was also faster compared to CO_2 and C_2H_6 molecules in the sII mixed hydrate, leading to changes in the hydrate composition throughout the process.

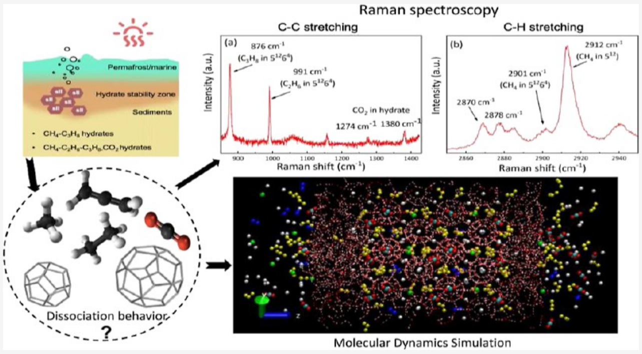

1. INTRODUCTION

Natural gas hydrates are non-stoichiometric crystalline substances where guest molecules like CH_4, C_2H_6, C_3H_8, CO_2, H_2S, etc. encase into cavities composed of hydrogen-bonded water molecules under elevated pressure and low temperature conditions.[1,2] Hydrate samples acquired from natural hydrate reservoirs have indicated three common structures—cubic structure I (sI), cubic structure II (sII), and hexagonal structure H (sH)—depending on the size of the involved guest molecule.[3,4] Small guests such as CH_4, C_2H_6, CO_2, or their mixtures with a proper composition often form sI hydrates,[5] consisting of two small pentagonal dodecahedra (5^{12}) cavities and six large tetrakaidecahedra ($5^{12}6^2$). In the presence of larger guest molecules like C_3H_8 or iso-C_4H_{10}, sII hydrates form. A unit cell of sII hydrates contains 16 small pentagonal dodecahedra (5^{12}) cavities and 8 large hexakaidecahedra ($5^{12}6^4$).[4] Structural H hydrates are only formed with even larger guests like neo-pentane when small gas molecules (e.g. CH_4) are available to occupy the small cavities.[6]

Natural gas hydrates have aroused considerable interests in terms of them being a promising energy resource, a potential geohazard, and a contributor to the global climate warming. Both recovering CH_4 gas from natural gas hydrate deposits and assessing the potential risks of CH_4 release require an accurate knowledge of the dissociation behavior of gas hydrates. Although CH_4 is overwhelmingly represented for natural gas hydrates, the fraction of other hydrocarbons like C_2−C_5 or CO_2 gas can not beneglected. Our previous effort (Part I[7]) dealt with the dissociation behavior of simple sI CH_4 hydrates in response to thermal stimulation and/or depressurization. While applying Raman spectroscopic and PXRD measurements together with molecular dynamics simulations, the results showed an oscillating behavior during the dissociation process, indicating different stages of the hydrate cavity breakup. Large $5^{12}6^2$ cavities in CH_4 hydrates break up faster than small 5^{12} cavities. However, it should be noted that sI hydrates showed different dissociation kinetics compared to sII hydrates.[8] Therefore, the composition of the hydrate phase is crucial for the evaluation of the sII hydrate dissociation process. A previous study from Tang et al. suggested that the

Received: November 24, 2022
Revised: February 10, 2023
Published: February 22, 2023

https://doi.org/10.1021/acs.energyfuels.2c03985
Energy Fuels 2023, 37, 4497−4514

hydrate cavities for $CH_4-C_3H_8$ hydrates collapsed as an entity with identical dissociation rates of both large and small cavities in a unit cell.[9] This was also supported by other researchers studying sI CH_4 hydrates[10] and sI CH_4-CO_2 mixed hydrates.[11] In contrast, Truong−Lam et al.,[12] who also worked on a $CH_4-C_3H_8$ system but with a different initial gas composition, reported a preferential dissociation of the small and large cavities filled with CH_4 compared to large cavities filled with C_3H_8. The variations in the experimental setups might be the cause of different conclusions. It should also be pointed out that gas hydrate dissociation was induced by depressurization and without a constant gas supply in these studies. Considering the controversial phenomenon addressed in previous studies, the dissociation behavior of mixed gas hydrates remains unclear. Moreover, little is known about the dissociation of multicomponent mixed gas hydrates even though they frequently occur in natural reservoirs.

Molecular simulation also implied that the full dissociation process can be complicated and is still poorly understood. Gas molecules are released from partially open cavities and closed cavities which break down layer by layer. The difficulty of gas diffusion in the hydrate-liquid side also causes a change in the dissociation rate and is considered as a rate-controlling stage in the hydrate dissociation process.[13−16] The reversible regrowth occurs at the interface and nucleates the water molecules around gas molecules in the liquid phase, thereby forming partial hydrate cavities.[17] In addition, the preferential dissociation of some cavity types due to specific guest properties and their distributions was previously observed.[15,18] Iwai et al. found that CH_4 hydrates were more stable than CO_2 hydrates under the calculated conditions.[15] Kondori observed different decomposition behaviors of hydrate systems with different compositions. The optimal configuration of sI binary hydrates according to molecular dynamic simulations was when CO_2 and CH_4 occupy the large $5^{12}6^2$ and small 5^{12} cavities, respectively. It was also found that the presence of CH_4 molecules in large cavities decreased the stability of sII hydrates for the mixtures of $CH_4-C_3H_8$, CH_4−iso-C_4H_{10}, and $CH_4-C_3H_8$−iso-C_4H_{10}.[18]

This study is an extension of Part I research (ef-2022-03984u) on the dissociation process of simple sI CH_4 hydrates. It explored the dissociation process of sII binary $CH_4-C_3H_8$ hydrates and sII $CH_4-C_2H_6-C_3H_8-CO_2$ mixed gas hydrates with regard to thermal stimulation. A series of *in situ* and *ex situ* Raman spectroscopic measurements were performed on hydrate crystals continuously, recording the molecular behaviors throughout the whole dissociation process. To investigate the microscopic details of the hydrate cavity breakup, molecular dynamics simulation (MD) was also carried out applying similar conditions as the experiments to understand the principles of the dissociation process, even though the time and space dimensions are not comparable to the experiments. To the best of the authors' knowledge, a combination of laboratory measurements and numerical modeling of mixed gas hydrate dissociation under similar conditions at micrometer-and nanometer-scales has been rarely reported. In addition, this study deals with sII hydrates containing a high percentage of higher hydrocarbons besides CH_4, which filled the gap in understanding the multicomponent gas hydrate system. Discussions based on both experimental simulation and MD simulation revealed a time-resolved information of the guest molecules during the dissociation process of sII gas hydrates and predicted the potential mechanisms behind the phenomenon.

2. METHODS

2.1. Experimental Section. Raman measurements were performed on a LabRAM HR Evolution instrument (Horiba Scientific), equipped with a microscope Olympus BX-FM, and a data acquisition system. A microscope objective lens with 20× magnification was selected for *in situ* Raman measurements, whereas a 50× objective was used for *ex situ* measurements. A frequency-doubled Nd/YAG solid-state laser ($\lambda = 532$ nm) was employed as the excitation source with an output power of 100 mW. Each spectrum collected,at a spectral resolution of 0.6 cm^{-1} under the selected condition, was obtained in 2 accumulations of 5 s exposure time. The analysis achieved a spatial resolution of ∼0.5 μm in $x-y$-directions and ∼1.5 μm in the z-direction at a maximum with the help of a motorized pinhole in the analyzing beam path. During the measurements, the pinhole size was set at 100 μm for *in situ* Raman measurements and 1000 μm for *ex situ* measurements, which offered best spatial resolutions. A silicon crystal which has a Raman shift at 521 cm^{-1} was applied as a reference standard for the calibration of the Raman spectra. *In situ* experiments were carried out in a custom-made high-pressure cell located on a Märzhauser Scan + sample stage which is motorized and software controlled. An additional Linkam cooling stage was used for the *ex situ* Raman spectroscopic analysis. More details regarding the Raman spectroscopy, the pressure cell, and data analysis can be found in our previous publication.[19]

Two gas mixtures were used in this study, with one containing only CH_4 and C_3H_8, and the other comprising four components: CH_4, C_2H_6, C_3H_8, and CO_2. For the formation of sII hydrates within the *in situ* experiments, 150 μL deionized water was first loaded into the high-pressure cell. The cell was sealed and pressurized at 3.0 MPa, 278 K (Figure 1), with continuous gas mixtures mentioned above. The incoming gas was pre-cooled so that it was in thermal equilibrium with the sample when it reached the cell. This, together with the extensive cooling of the cell and the small sample volume, ensures that a thermal gradient within the sample can be excluded and thermal equilibrium is achieved rapidly. Hydrate crystals were continuously analyzed during the formation process in $x-y$ directions using Raman spectroscopy to help identify the guest compositions. When there was

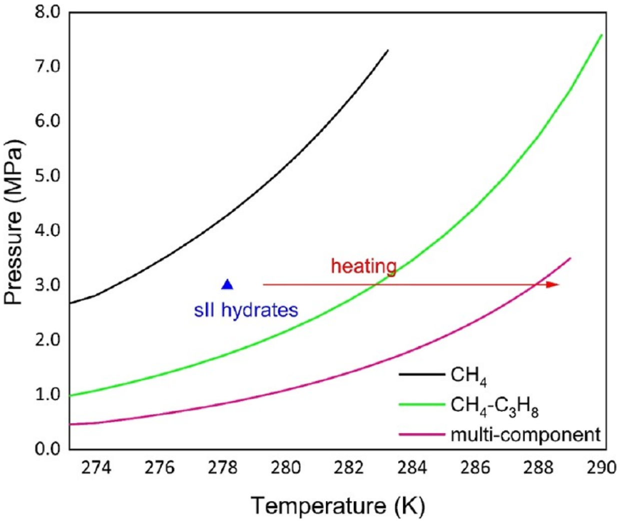

Figure 1. Equilibrium curves for sI CH_4 hydrates, sII binary hydrates, and multicomponent mixed gas hydrates calculated from the software CSMGem[4] and the corresponding experimental p−T condition for the *in situ* Raman measurements for sII hydrates at 3.0 MPa, 278 K (blue triangle).

an indication of a steady state showing that the composition and cavity occupancy of the hydrate phase were maintained for hours, the temperature was gradually increased until the mixed gas hydrates dissociated. Further Raman analysis of the dissociation process were made stepwise at 280 K, 281 K, 281.5 K, 282 K, 282.5 K, 283 K, 283.5 K and 284 K, respectively, for the binary CH_4−C_3H_8 hydrates and at 281 K, 284 K, 286 K, 287 K, 287.5 K, 288 K and 288.5 K for the complex mixed hydrates. It should be noted that each temperature step was maintained for at least 20 mins to achieve thermal equilibrium in the system. Selected hydrate crystals were continuously monitored at each temperature step.

In addition, both CH_4−C_3H_8 hydrates and multicomponent gas hydrates were synthesized in batch pressure vessels from the aforementioned gas mixtures and ice powder for *ex situ* Raman measurements. Fine-grained ice with a size range of around 10 μm was generated by spraying deionized water into a liquid nitrogen bath and was then grounded in a 6750 Freezer Miller (SPEX CertiPrep). The prepared ice powder was placed into the vessels for pressurization with the respective gas mixture at 3.5 MPa and kept in a freezer at around 266−269 K. Due to the enclathration of gas molecules, the pressure of the vessels decreased significantly at the beginning. After several weeks, the vessels were depressurized, and samples were transported to the Linkam stage at atmospheric pressure and 168 K. To start the dissociation of hydrates, the system was steadily heated up by 4−5 K every 10 mins until hydrate dissociation was observed. A series of Raman measurements were carried out with the same spectrometer at selected points on the hydrate phase, thus providing information about the hydrate composition at the specific point throughout the process until a complete dissociation of the hydrates. A replication experiment was conducted under identical conditions and with same gas mixtures. The original experimental data set can be found through GFZ Data Services.[20]

2.2. Molecular Dynamics Simulation Details. The molecular dynamics simulations were performed by using the GROMACS program (version 2018.8).[21] The dissociation process of mixed gas hydrates was studied using two different configurations: 2 × 2 × 4 unit cell replica of sII binary (CH_4 + C_3H_8) hydrates and sII mixed (CH_4 + C_2H_6 + C_3H_8 + CO_2) hydrates with a dimension of 3.54 nm × 3.54 nm × 7.11 nm. In MD simulation, a small portion of the hydrate crystal observed in the experiment was considered to investigate how the dissociation process occurs from the hydrate surface to the depth. The initial configuration of the simulation boxes is shown in Figure 2. The initial coordinates of the atoms in the unit cells were obtained from the work of Takeuchi et al. that presented the optimized configurations for the hydrate structures.[22] Initial gas compositions were approximated as the equilibrium compositions of the mixed hydrate phases calculated with CSMGem software at 278 K and 3.0 MPa[4] and shown in Table 1. In the case of the multicomponent gas system, CO_2 in $5^{12}6^4$ cavities and C_2H_6 in 5^{12} cavities were neglected because of their low mole fraction according to CSMGem calculations. To allow the calculation of the large-to-small cavity ratio for CH_4 molecules and to be more comparable to the experimental results, one large cavity was occupied by CH_4. In this context, it should also be noted that not all small cavities were occupied by a gas molecule.

The hydrate phases were placed in the center of the simulation box of around 3.54 nm × 3.54 nm × 10 nm (Figure 2) with vacuum on each side of the hydrate in the *z*-direction to provide free interfaces on which the heterogeneous decomposition was initiated. The periodic boundary conditions were used in three directions.

The intermolecular interactions of water molecules were modeled with the TIP4P/Ice model,[23] while CO_2 and hydrocarbon molecules were represented by TraPPE[24] and TraPPE united atom[25] potentials, respectively, all of which keep the internal structures of the molecules rigid by using the LINCS algorithm.[26] The force field parameters are given in Table 2. The Lorentz−Berthelot combining rules were adopted for unlike pairs of atoms in particular, $\varepsilon_{ij} = (\varepsilon_{ij}\varepsilon_{jj})^{1/2}$ and $\sigma_{ij} = (\sigma_{ij} + \sigma_{jj})/2$.[27] A cutoff of 1.4 nm was applied for the short-range van der Waals interactions, and the long-range electrostatic interactions were also handled using the Particle Mesh Ewald method[28,29] with a relative error of 10^{-6}.

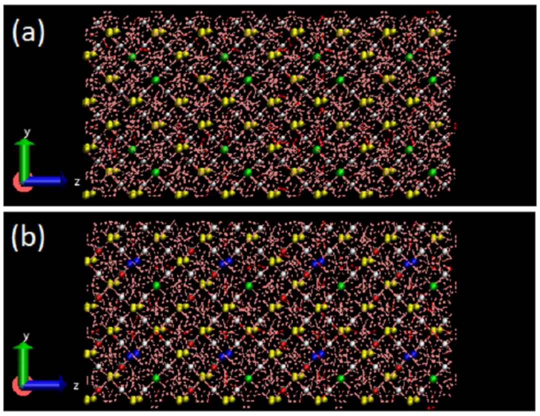

Figure 2. Initial configuration of the simulation boxes on the (100) surface used in this work. (a) 2 × 2×4 slab of sII CH_4 + C_3H_8 hydrates and (b) 2 × 2×4 slab of sII mixed gas (CH_4 + C_2H_6 + C_3H_8 + CO_2) hydrates. The simulations had free surfaces in the *z*-direction. The hydrogen-bonded water network in the clathrate hydrate is shown by the red lines. CH_4 in the small cavities, CH_4 in the large cavities, and C_2H_6, C_3H_8, and CO_2 molecules are shown in white, green, blue, yellow, and cyan-red, respectively. Each cavity contains a maximum of one gas molecule.

The temperature and pressure of the simulation were kept constant using a Berendsen thermostat and barostat[30] by the *NPT* ensemble. The MD integrator of the Leap-frog algorithm[31] was used for the integration of the equations of motion at each time step of 2 fs. The decomposition of sII hydrate systems was simulated at the starting temperature of 278 K and a pressure of 3.0 MPa. The temperature of the system was increased stepwise up to 323 K until the dissociation of the hydrate phase was totally completed, following the same methodology as the experimental simulations. Figure S1 in the Supporting Information shows the changes in the temperature of the simulation runs.

For quantitatively characterizing the dissociation process, the F_3 order parameter was used for quantifying the local arrangement of water molecules at different locations of the hydrate phase[32] that is defined as

$$F_{3,i} = \langle [\cos\theta_{jik}|\cos\theta_{jik}| + \cos^2 109.47]^2 \rangle_{j,k} = \begin{Bmatrix} 0.1 \text{ liquid water} \\ 0.0 \text{ solid water (ice, hydrate)} \end{Bmatrix} \quad (1)$$

where θ_{jik} shows the angle between three oxygen atoms of water molecules which are close together so that atom *i* is in the center of a spherical shell of 0.35 nm including atoms *j* and *k*. From the equation, the F_3 order parameter would be around zero if the highly tetrahedral structures like ice and clathrate hydrate are present in the system and its value reaches ~0.1 for liquid water. The F_3 parameter gradually increases as the hydrate crystals are dissociated during the simulation trajectory. For quantifying the spatial extent of hydrate dissociation, the initial hydrate phases were divided into different layers parallel to the *z*-direction and the F_3 parameter was individually calculated for each layer. All simulation data are available through GFZ data services.[33]

3. RESULTS AND DISCUSSION

3.1. sII CH_4−C_3H_8 Hydrates—Raman Spectroscopic Investigations. In the first step of the experiment, the pure gas phase was analyzed through *in situ* Raman spectroscopy. The results are shown in Figure 3(a,b). Raman band at 2917 cm^{-1} represents CH_4 molecules in its gas phase, while the band

Table 1. Gas Compositions in sII Hydrate Phase Used in This Work Calculated at 278 K and 3.0 MPa

Gas phase	Gas component	Feed gas[a] (%)	Fractional cavity occupancy CSMGem		Number of gas molecules in the unit cell—This work	
			Small cavity	Large cavity	Small cavity	Large cavity
Binary (CH_4 + C_3H_8)	CH_4	94.8	0.8530	0.2137	14	2
	C_3H_8	5.2	0.0000	0.7736	0	6
Multicomponent (CH_4 + C_2H_6 + C_3H_8 + CO_2)	CH_4	44.3	0.6045	0.0059	10	1
	C_2H_6	19.7	0.0026	0.1015	0	1
	C_3H_8	20.7	0.0000	0.8858	0	6
	CO_2	15.3	0.1763	0.0060	3	0

[a] The feed gas composition was obtained from Raman spectroscopic measurements.

Table 2. Force Field Parameters for Water (TIP4P/Ice),[23] Hydrocarbons (TraPPE-UA),[25] and CO_2 (TraPPE)[24] Used in This Work

Atom	σ/nm	ε/kcal·mol^{-1}	q/e
O (H_2O)	0.3167	0.2108	0.0000
H (H_2O)			0.5897
M (H_2O)			−1.1794
C (CH_4)	0.3730	0.2941	0.0000
CH_3 (C_2H_6)	0.3750	0.1947	0.0000
CH_2 (C_3H_8)	0.3950	0.0914	0.0000
CH_3 (C_3H_8)	0.3750	0.1947	0.0000
C (CO_2)	0.2800	0.0536	0.7000
O (CO_2)	0.3050	0.1569	−0.3500

at 869 cm^{-1} can be recognized as C_3H_8 in the gas phase. The gas composition was determined from the calculations of the corrected integrated intensities of these two Raman bands, which were 94.8 mol % CH_4 and 5.2 mol % C_3H_8.

Raman spectroscopy is a very good method to detect the formation of gas hydrates, since the position of the bands for molecules enclosed in the hydrate is shifted compared to the position of the Raman bands for free gases, as indicated in Figure 3c−d. A prominent Raman band at 876 cm^{-1} can be attributed to the C−C stretching vibrations of C_3H_8 encased in the large cavities of sII hydrates, while the bands at 2902 and 2912 cm^{-1} indicated CH_4 in the large $5^{12}6^4$ and the small 5^{12} cavities of sII, respectively. The integrated intensities of the relative Raman bands were used to semi-quantify the hydrate composition. Noteworthy, only sII hydrates were detected with the enclathration of both CH_4 and C_3H_8 in the hydrate cavities. Right after the hydrate system achieved a steady condition, in which the hydrate composition and cage occupancy remained stable at least for several hours, the system was heated up by increasing the temperature stepwise to stimulate hydrate dissociation.

When C_3H_8 content achieved 45.6 mol % in the hydrate phase, the average concentration of CH_4 reached 54.4 mol % for the chosen crystals before the dissociation process started, indicating a preferential incorporation of C_3H_8 molecules in the large cavities of sII hydrates based on the statement that C_3H_8 molecule was not capable of fitting into the small (5^{12}) cavities due to its large size.[34] Figure 4 depicts the compositional changes of C_3H_8 and CH_4 in the hydrate phase with increasing temperature during dissociation. There was a turning point at 283 K, before which the composition remained almost unchanged. However, a greater variation of the hydrate composition was observed after 283.5 K, a temperature close to the equilibrium temperature at 3.0 MPa, suggesting the beginning of hydrate decomposition. With higher temperatures, the relative CH_4 concentrations in some of the measuring points were reduced, while the relative content of C_3H_8 was increased. The results suggested a faster release of CH_4 from hydrate cavities than that of C_3H_8 molecules. The morphological alterations seen on each crystal surface coincided with the changes in the hydrate compositions. Consider one crystal in Figure 5 as an illustration. Up until 283.5 K, the morphological appearance of the hydrate crystal essentially remained unchanged. The hydrate crystal lost its even surface and sharp edges at a temperature of 283.5 K, same as the temperature turning point of the hydrate composition. The entire structure collapsed at 284 K.

As indicated from Figure 3d, Raman signals for CH_4 in the gas phase (2917 cm^{-1}) were close to the Raman bands of CH_4 in the small (5^{12}) cavities (2912 cm^{-1}). The determination of the integrated intensities of these two Raman bands from *in situ* measurements can become unreliable, especially at lower intensities. Therefore, additional *ex situ* Raman measurements with no coexisting gas phase were conducted to provide a more precise calculation of the large-to-small cavity ratio.

Ex situ Raman measurements revealed that the hydrate phase composition reached 75.8 mol % CH_4 and 24.2 mol % C_3H_8 before dissociation, much closer to the calculated composition from CSMGem (Table 3). Changes of the hydrate composition shown in Figure 6a also suggested a varied behavior of CH_4 and C_3H_8 molecules. Similar to the trend observed from *in situ* Raman measurements (Figure 4), there was a significant decrease in the CH_4 concentration of the hydrate after 110 mins at a temperature of 215 K, accompanied by an obvious increase in the relative C_3H_8 concentration. It is worth mentioning that the hydrate composition started to change at a temperature (215 K) much lower than the equilibrium temperature for CH_4−C_3H_8 hydrates at ambient pressure (236 K) as calculated from CSMGem.[4]

The calculation of the large-to-small cavity ratio was based on the results obtained from *ex situ* Raman measurements applying the eq 2, taking into account that CH_4 occupied both small 5^{12} and large $5^{12}6^4$ cavities of sII, while C_3H_8 only incorporated into the large $5^{12}6^4$ cavities.

$$\text{Large} - \text{to} - \text{small cavity ratio} = \frac{\frac{A\ \text{at}\ 2902\ \text{cm}^{-1}}{\sigma 1} + \frac{A\ \text{at}\ 876\ \text{cm}^{-1}}{\sigma 2}}{\frac{A\ \text{at}\ 2912\ \text{cm}^{-1}}{\sigma 1}} \qquad (2)$$

where A represents the integrated intensity of the specific Raman band which can be obtained from the Raman spectrum; σ_1 is the relative Raman scattering cross-sectional factor for CH_4 (σ_1 = 8.63) and σ_2 is for C_3H_8 (σ_2 = 1.6).[35,36]

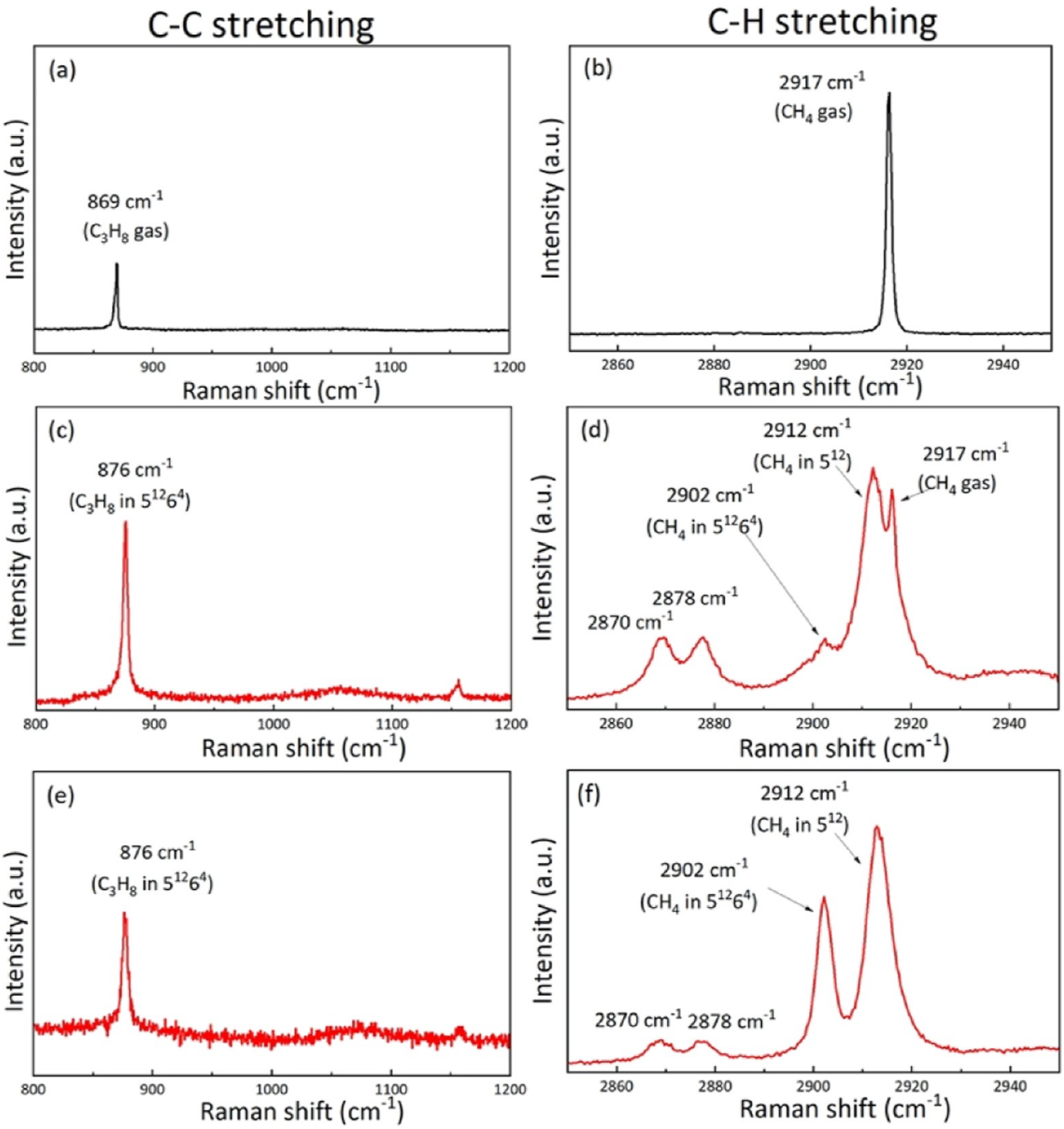

Figure 3. Raman spectra of gas phase (−b) and binary hydrate phase from *in situ* measurements (c−d) and *ex situ* measurements (e−f) in the C−C stretching vibrational interval from 800 cm^{-1} to 1200 cm^{-1} and the C−H stretching vibrational region from 2850 cm^{-1} to 2950 cm^{-1}.

It turned out that the initial large-to-small cavity ratio in the specific hydrate crystal was around 0.7−0.8 (Figure 6b). Notably, one unit cell of sII hydrates contains 16 small 5^{12} cavities and 8 large $5^{12}6^4$.[4] The value higher than 0.5 indicated that around 5−6 small cavities were left empty. As the experiment proceeded, the ratio of large-to-small cavities showed an increasing trend which might be attributed to a faster release of CH_4 from the small 5^{12} cavities as compared to those from large $5^{12}6^4$ cavities (Figure 6b). Due to a relatively low signal-to-noise ratio at the end of the experiments, further analysis was carried out excluding the last few data points, assuming that the hydrate concentration was rather low at that time. Results from the repeated test are shown in the Supporting Information Figure S2, separately. It is also worth mentioning that an opposite trend related to the large-to-small cavity ratio was observed for the sI CH_4 hydrates as reported in Part I of our research (ef-2022-03984u), in which the ratio dropped over time.

3.2. sII CH_4−C_3H_8 Hydrates—Molecular Dynamics Simulation.

The simulation results of the binary sII hydrate dissociation were obtained at 3.0 MPa and a starting temperature of 278 K. This system was also gradually heated up until the hydrates were completely decomposed at 323 K. Figure 7 shows the snapshots of the hydrate dissociation on the (110) surface as well as the *z*-density profiles for both CH_4 and C_3H_8 molecules during the simulation. Similar to that observed for sI hydrates in Part I (ef-2022-03984u), the layered dissociation of hydrate from the outermost layers to the inner ones happened in the direction parallel to the hydrate interface. There were some incomplete open cavities at the hydrate surface that could promote the decomposition so that gas molecules easily escaped from them. Then, the complete

https://doi.org/10.1021/acs.energyfuels.2c03985
Energy Fuels 2023, 37, 4497−4514

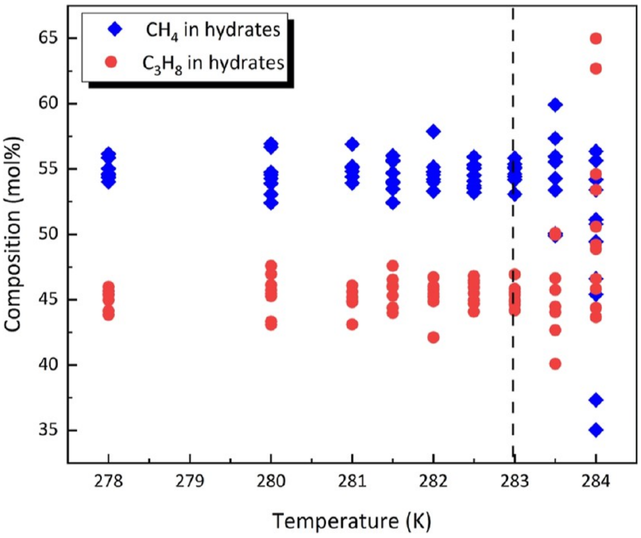

Figure 4. Changes of hydrate composition regarding the concentration of CH_4 (blue diamonds) and C_3H_8 (red circles) during the dissociation process from *in situ* Raman spectroscopic measurements. The equilibrium temperature for the chosen $CH_4-C_3H_8$ hydrates at 3 MPa was calculated from CSMGem and indicated by the black dashed line.

Table 3. Comparison of the Original Feed Gas Composition, $CH_4-C_3H_8$ Hydrate Composition at a Steady State, and the Calculated Hydrate Composition at Equilibrium from CSMGem at 3.0 MPa, 278 K

	Composition (mol %)	
Phase	CH_4	C_3H_8
Original gas (measured)	94.8	5.2
$CH_4-C_3H_8$ mixed gas hydrates (*in situ*)	54.4	45.6
$CH_4-C_3H_8$ mixed gas hydrates (*ex situ*)	75.8	24.2
$CH_4-C_3H_8$ mixed gas hydrates (CSMGem)	70.8	29.2

hydrate cavities started to collapse and gas molecules were released. The animation from the trajectories of the simulation is also given in the Supporting Information Animation S1. From the z-density profiles, the distribution of CH_4 and C_3H_8 in the system along the z-direction of the simulation box could be realized. The periodic peaks from z = ∼1.7 to ∼8.3 nm at the initial configuration indicated that the gas molecules existed from the hydrate cavities; however, these peaks gradually disappeared from the two ends of the hydrate phase. It should be noted that gas molecules are not homogeneously distributed throughout the unit cell and thus the box; therefore, their z-density profiles appear to be irregular. As the dissociation proceeded, the phases of liquid and gas were formed so that the liquid phase was located between the hydrate and gas phases. The density of gas molecules in the liquid phase was very low, while it increased in the gas phase until the end. So, it could be used to qualitatively show how much hydrates were left. At the gas–liquid interface, the excess gas density was observed compared to the bulk gas phase which was a reflection of the wetting behavior of gas on the water surface.[37]

The time evolution of the F_3 order parameter upon increasing the temperature of the system for different cross sections of the slab of the CH_4 + C_3H_8 hydrate parallel to the z-direction is shown in Figure 8. As mentioned in Section 2.2, the F_3 order parameter is a measure of the order in the crystalline structure. It would be around zero (= <0.02) for the clathrate hydrates. A value increase indicates a dissolution of the crystal structures. The heterogeneous layer-by-layer decomposition of hydrates was also reported in the literature[38,39] due to the asymmetric surfaces of the hydrate.

At the starting temperature of 278 K, the outermost layers (with incomplete cavities) were partially decomposed as indicated by the increase of F_3 up to ∼0.03–0.04, implying that the water molecules at these layers were in a liquid-like amorphous phase. After around 10 ns, at a temperature of 284 K, the outermost layers of 1 and 8 started dissociating, and they were completely collapsed reaching the F_3 values of ∼0.07 at around 22 ns. The temperature of 284 K was ∼1 K above the equilibrium temperature at 3.0 MPa of sII CH_4 + C_3H_8 hydrate, as shown in Figure 1. It should be noted that the hydrate structures defined for the molecular dynamics simulation may not dissociate at the same temperature compared to those obtained from the experimental observations or calculated from the software, since some physical differences between experimental and simulation conditions affect these properties. However, small or significant shifts in the dissociation temperature of the gas hydrate systems from the experimental and theoretical measurements were previously observed in some MD works, which seems to be related to the simulated box, the potential of the molecules, etc.[40]

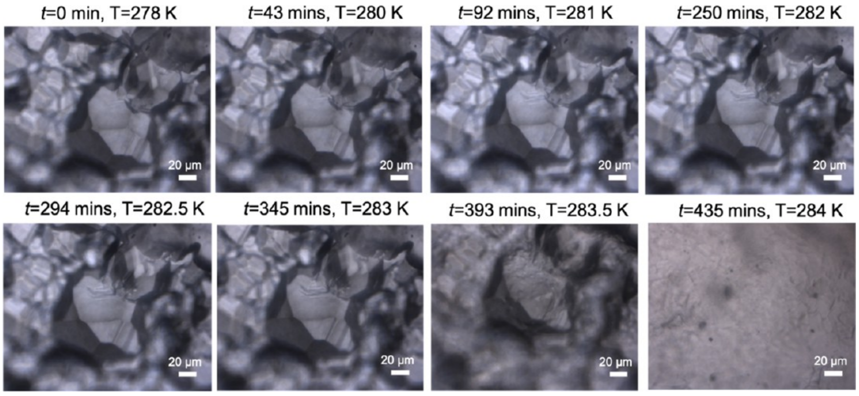

Figure 5. Illustration of the surface morphological changes of one selected hydrate crystal during the dissociation process from *in situ* Raman measurements.

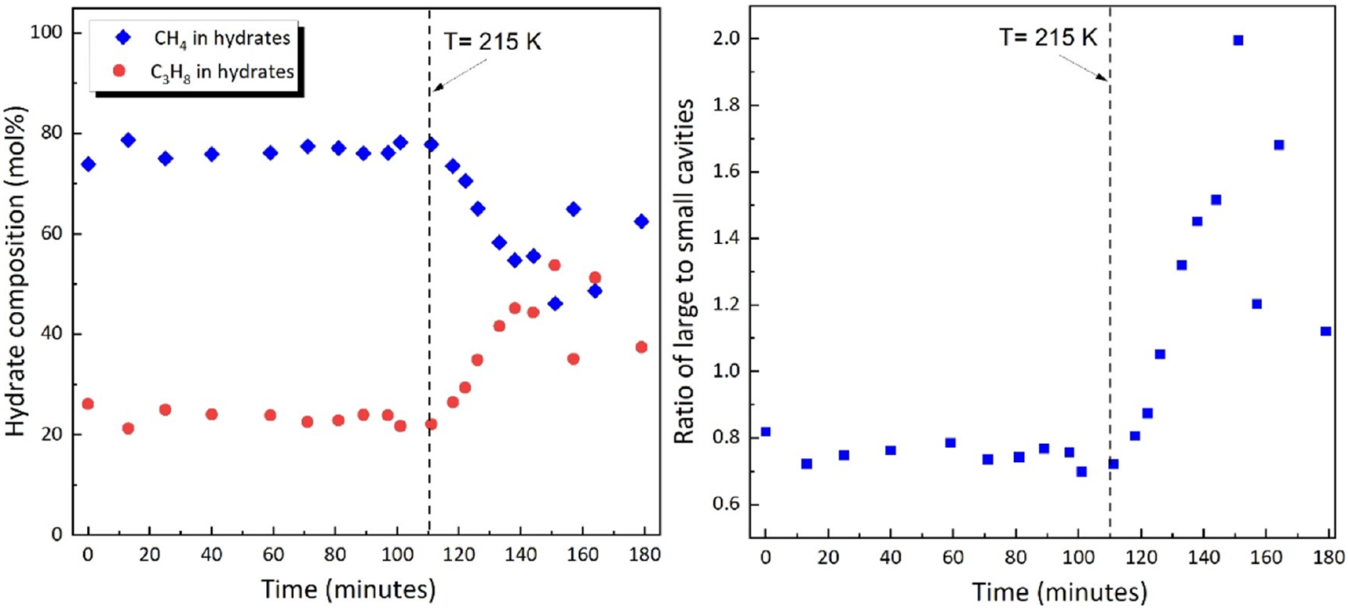

Figure 6. (a) Variation of the hydrate composition throughout the dissociation process from *ex situ* Raman measurements on a specific hydrate crystal at ambient pressure. (b) Large-to-small cavity ratio for both CH$_4$ and C$_3$H$_8$ molecules in the hydrate phase. The initial temperature was 168 K, and it increased by 4−5 K every 10 mins. The black dashed lines indicate the starting point (t = 110 min) of changes in the hydrate composition and the ratio of large-to-small cavities at T = 215 K.

After dissociation of the outermost layers which is accompanied by the release of gas molecules and the formation of an aqueous phase, the inner layers 2 and 7 started to dissociate but at a very slow dissociation rate. The formation of an aqueous phase decelerated the dissociation of the inner hydrate layers and the gas diffusion. Over time, this liquid phase thickened. After about 80 ns at 308 K, the decomposition process accelerated, and finally, at 323 K, the F_3 values of the last inner hydrate layers changed rapidly and approached a constant value of ∼0.08 after approximately 225 ns.

Figure 9 shows the time-resolved large-to-small cavity ratio for both CH$_4$ and C$_3$H$_8$ molecules that remained in the hydrate phase as well as the hydrate conversion. The hydrate conversion was calculated by dividing the number of remaining hydrate cavities by the initial number of hydrate cavities as a percent, indicating the amount of the gas hydrate converted to water and gas phases. The large-to-small cavity occupancy ratio is one of the computational measurements by which we could provide a comparison between the MD simulations and laboratory data.

From Figure 9, before the dissociation of the first layer, up to ∼10 ns, the large-to-small cavity occupancy ratio decreased, starting from ∼0.57, which was consistent with the 8:14 large-to-small occupancy cavity ratio designed for the sII unit cell as shown in Table 1. This corresponded to the dissociation of incomplete open cavities at the surfaces. It can also be seen that the hydrate conversion remained constant in this period. Thereafter, the large-to-small cavity ratio showed a slight oscillating behavior during the dissociation process. When the decomposition of two outermost layers happened (Figure 8), the large-to-small cavity ratio increased between around 10 and 22 ns, reaching up to a value of ∼0.6, implying that gas molecules in small cavities were released faster than those encased into the large cavities (marked as stage A). Afterward, the large-to-small cavity ratio returned to the theoretical value, while the hydrate conversion almost stagnated. However, the ratio increased again (marked as stage B) after ∼93 ns and the hydrate conversion decreased upon the dissociation of the first inner layers (see Figure 8). The ratio of the large-to-small cavity occupancy almost continuously increased until a simulation time of ∼200 ns. It implied that the small cavities were also decomposed faster upon dissociation of the inner layers. When all layers of the hydrate cell were totally decomposed, the data were really scattered and suddenly dropped, reaching zero, and so they were ignored for further interpretation.

Similar to those obtained for the sI CH$_4$ hydrates in Part I (ef-2022-03984u), there was no general trend for the large-to-small cavity ratio, and it showed an oscillating behavior during the dissociation process of binary sII hydrates as well. It seemed that the ratio increased upon dissociation of the layers, but when the hydrate conversion remained constant, it seemed to return to the theoretical value. During this phase, the formation of partial hydrate cavities in the liquid phase resulted in temporary stopping of the dissociation process. Figure 10 shows the snapshots of the CH$_4$ + C$_3$H$_8$ hydrate simulation to confirm the recrystallization of hydrate cavities during the dissociation process. These partial cavities were usually formed in the vicinity of the hydrate surface due to the high concentration of the gas molecules in this region. This is in agreement with those previously observed in the related literature.[14,17]

In the experimental section, the increasing of large-to-small cavity occupancy ratio during the decomposition of sII hydrates was also observed when the process approached the end (see Figure 6b). However, the same phenomenon was observed via MD simulation when the inner layers of the hydrate slab were dissociating. So, the two stages of A and B, as defined in Figure 9, could be the rate-controlling stages in the hydrate breakup of sII hydrates.

The composition of gas molecules in the hydrate phase during the dissociation process of the sII CH$_4$ + C$_3$H$_8$ hydrate is shown in Figure 11. This is another computational

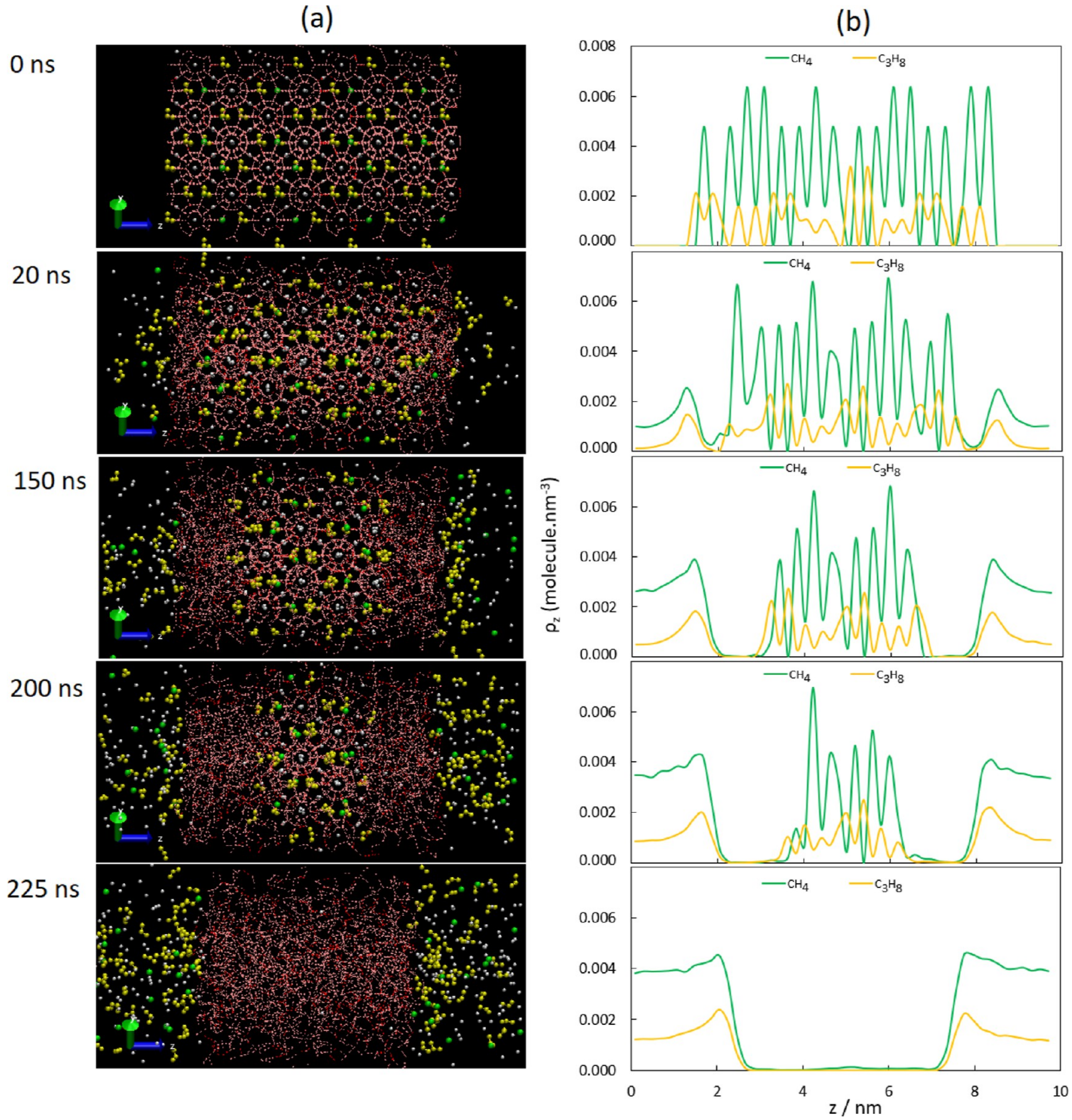

Figure 7. (a) Snapshots of the sII CH_4 + C_3H_8 hydrate dissociation on the (110) surface at different times in the simulation trajectory. The hydrogen bonding in the hydrate phase is shown in red. CH_4 in the small cavities, CH_4 in the large cavities, and C_3H_8 molecules are shown in white, green, and yellow, respectively. Each occupied hydrate cavity contains only one gas molecule. (b) The *z*-Density profile for CH_4 and C_3H_8 molecules during the dissociation process.

parameter to compare with the laboratory data. As seen in the figure, the relative CH_4 concentration decreased during the hydrate breakup, while the relative proportion of C_3H_8 in the hydrate phase generally increased, indicating the preferential dissociation of the cavities due to specific guest properties and their cage occupancy.

3.3. sII Multi-Component Mixed Hydrates—Raman Spectroscopic Investigations. The dissociation behavior of the multicomponent gas hydrates was significantly more complex. The initial gas phase composition was determined from *in situ* Raman spectroscopic measurements, which was 44.3 mol % CH_4, 19.7 mol % C_2H_6, 20.7 mol % C_3H_8, and 15.3 mol % CO_2. The formed sII hydrate phase achieved an average composition of 41.9 mol % CH_4, 9.1 mol % C_2H_6, 40.4 mol % C_3H_8, and 9.6 mol % CO_2 (Table 4), meanwhile exhibiting a high heterogeneity among crystals. To characterize the inhomogeneous nature of hydrates, Raman hyperspectral area mapping was applied focusing on the surface of one single hydrate crystal (Figure 12a). The ratio of CH_4 and CO_2

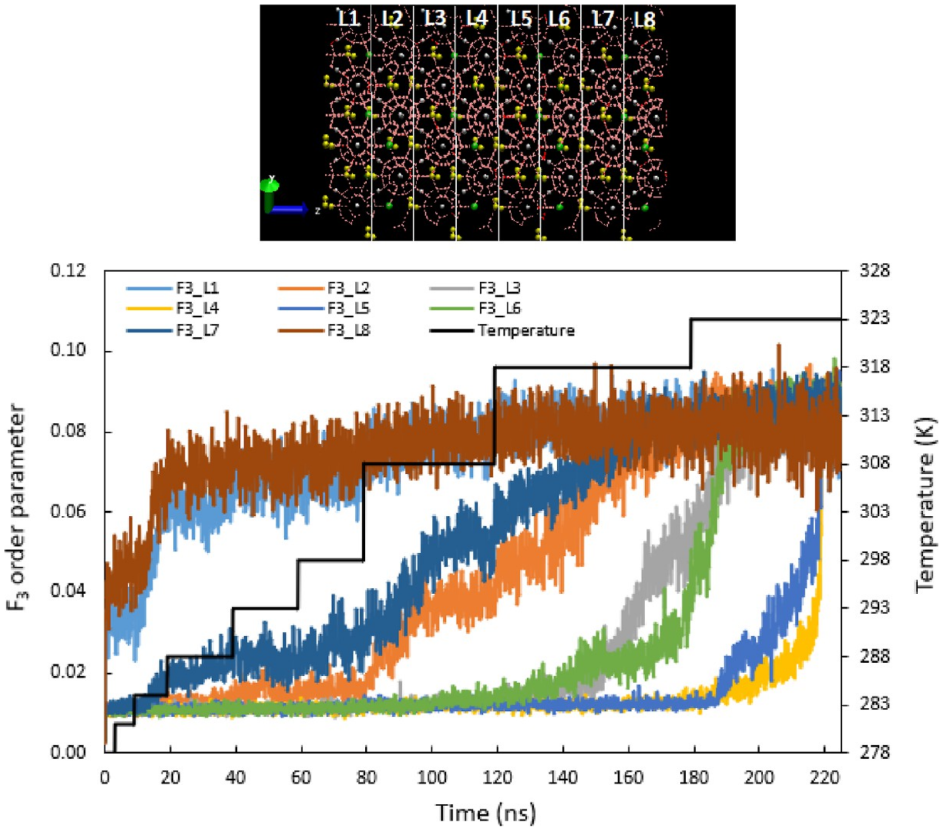

Figure 8. F_3 order parameter for the layered (CH_4+C_3H_8) hydrate slab along the z-direction. As shown, the hydrate phase was divided into eight layers, each with a thickness of around 0.875 nm and layers 1 and 8 forming the outermost layers with incomplete cavities.

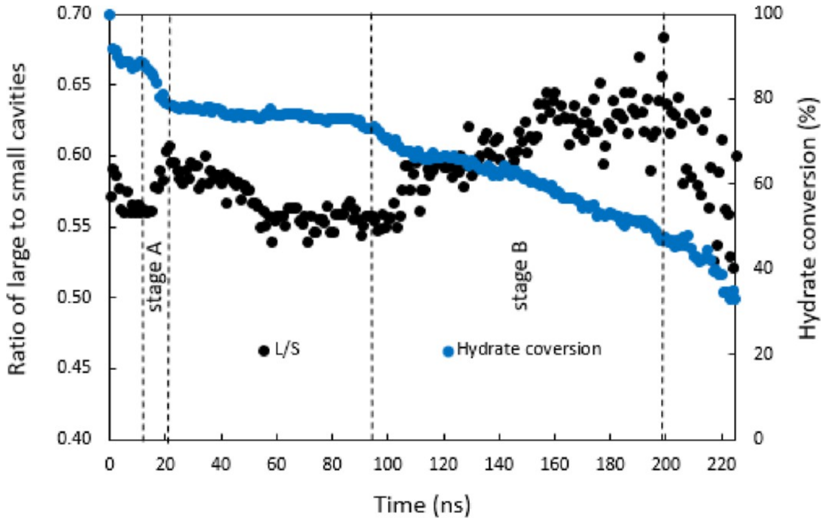

Figure 9. Ratio of large-to-small cavities in the hydrate phase as well as the hydrate conversion versus time for the sII CH_4 + C_3H_8 hydrate dissociation at p = 3.0 MPa and T = 278−323 K.

concentrations was adopted for a better clarification and is shown in a color-coded map (Figure 12b).

Figure 13 summarizes the surface morphological changes throughout the dissociation process from microscopic observations. As can be seen from the first snapshot, the hydrate crystal has a well-developed structure with sharp edges and a relative even surface. Several cracks were randomly distributed on the crystal surface, separating it into smaller parts. As the dissociation proceeded, the contours of the original crystal remained, but more cracks can be detected on the surface, providing evidence of the ongoing process. At T = 287.5 K, the edges of the hydrate crystal became indistinguishable, which clearly indicated the start of the dissociation. The hydrate crystal lost its original contours when the temperature reached 288 K, releasing gas bubbles from hydrate cavities. After the temperature was increased to T = 288.5 K, the hydrate phase was totally dissociated.

Detailed analyses from *in situ* Raman measurements on the dissociation of sII mixed gas hydrates at different temperature conditions are discussed in Figures 14 and 15. The Raman

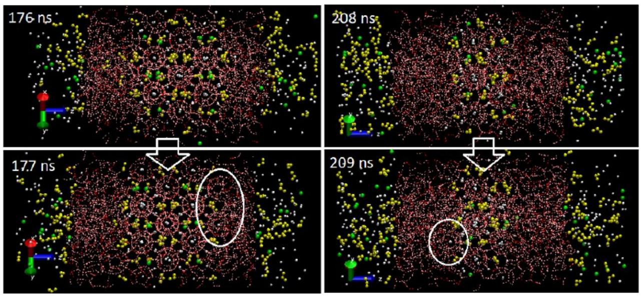

Figure 10. Snapshots of CH_4 + C_3H_8 hydrate simulation on the (110) surface showing the recrystallization of hydrate cavities during the dissociation process. White circles show the recrystallized hydrate cavities.

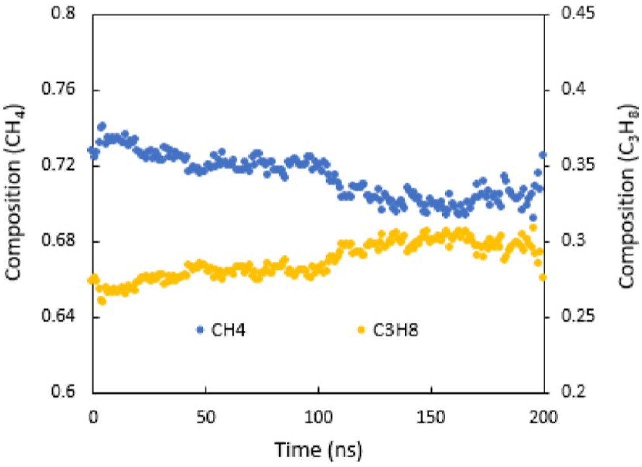

Figure 11. Relative composition of gas molecules in the hydrate phase versus time for the sII CH_4+C_3H_8 hydrate dissociation.

Table 4. Comparison of the Original Feed Gas Composition, Multi-Component Gas Hydrate Composition at a Steady State, and the Calculated Hydrate Composition at Equilibrium from CSMGem at 3.0 MPa, 278 K

	Composition (mol %)			
Phase	CH_4	C_2H_6	C_3H_8	CO_2
Original gas (measured)	44.3	19.7	20.7	15.3
Multicomponent gas hydrates (*in situ*)	41.9	9.1	40.4	9.6
Multicomponent gas hydrates (*ex situ*)	37.1	10.7	37.2	15.0
Multicomponent gas hydrates (CSMGem)	47.3	4.2	34.5	14.0

bands at 876 cm^{-1} and 991 cm^{-1} can be assigned to the C−C stretching mode region for C_3H_8 and C_2H_6 incorporated into the sII large $5^{12}6^4$ cavities, respectively. The occurrences of their corresponding gas peaks were presented at 869 cm^{-1} and 993 cm^{-1}. Two bands at 1274 cm^{-1} and 1380 cm^{-1} were referred to as the double Fermi diads of CO_2 molecules in the hydrate phase (Figure 14b),[41] while the smaller Raman bands at 1285 cm^{-1} and 1388 cm^{-1} were attributed to gaseous CO_2. Unfortunately, it was impossible to distinguish CO_2 in large $5^{12}6^4$ or small 5^{12} cavities of sII hydrates from Raman spectra. The C−H stretching of C_3H_8 molecules in sII large cavities was determined to be at approximately 2870 cm^{-1} and 2878 cm^{-1} in Figure 14c. CH_4 in the small 5^{12} cavities of sII hydrates and the gas phase was observed by the C−H stretching modes at 2912 cm^{-1} and 2917 cm^{-1}, respectively. The Raman band for CH_4 in the large $5^{12}6^4$ cavities had a position of approximately 2901 cm^{-1}, depicted as a small shoulder near the band at 2912 cm^{-1} (Figure 14c). In contrast to other sII hydrates with less guest components,[42−44] the Raman bands of CH_4 in both small 5^{12} and large $5^{12}6^4$ cavities in this study showed a slight red shift due to the effects of higher hydrocarbons in neighboring cavities on the CH_4 molecules. The O−H stretches of water formed a broad spectral feature from around 3000 cm^{-1} to 3600 cm^{-1} (Figure 14d). A large maximum occurred at around 3160 cm^{-1} which can be attributed to the increased hydrogen bonding in the clathrate structures.[45] Figure 14 demonstrates that the Raman band intensity was remarkably similar at 281 K as compared to that at 278 K. However, the intensities declined with time as the system warmed up progressively. At T = 288 K, Raman spectroscopic investigations only identified trace levels of C_3H_8, C_2H_6, and CO_2 in the hydrate structures. CH_4 molecules were largely liberated from the hydrate structures, especially the small cavities as indicated by the significant drop in the intensity of the Raman band at 2012 cm^{-1}, with the small "shoulder" at 2901 cm^{-1} no longer recognizable. The intensity decrease of the Raman band at 3160 cm^{-1} also indicated that the number of well-structured hydrogen-bonded water molecules decreased, suggesting a breakdown of the crystalline structure when the temperature increased to 288 K.

The relative composition of the hydrate phase was calculated through the concentration of each guest molecules and the results from one of the tests are shown in Figure 15. Extraordinary variations beyond the normal fluctuations were observed at higher temperature steps (287.5 and 288 K), due to the varied dissociation behaviors of different hydrate crystals. In addition, the CH_4 content in the hydrate phase declined at temperatures above 286 K, while the relative concentrations of C_2H_6 and CO_2 slightly increased. The C_3H_8 level increased in some crystals, while it decreased in others.

Similar to the sII binary system, it was also difficult to differentiate CH_4 in small 5^{12} cavities of the sII hydrate (2912 cm^{-1}) and in the gas phase (2917 cm^{-1}) from *in situ* Raman measurements (Figure 14); thus, further analysis was discussed based on the results from *ex situ* measurements (Figure 16). Figure 17a exhibits the time-resolved hydrate composition from *ex situ* Raman spectroscopic measurements obtained on one selected crystal. It was clear that the CH_4 content in the hydrate declined after around 140 mins, while C_2H_6 and CO_2 showed an upward trend, which was in agreement with the observations from *in situ* measurements (Figure 15). In contrast to the findings from *in situ* measurements, the C_3H_8 concentration displayed an upward trend as well at the end of the dissociation process. Similar to the binary system, an early start of dissociation within the stability field was also observed from *ex situ* Raman measurements of the mixed gas hydrate system (228 K vs of 245 K calculated with CSMGem). The comparison of the hydrate composition from *in situ* and *ex situ* measurements, gas phase measurements, and software calculation is shown in Table 4. According to the calculation from CSMGem (Table 1), the fractional cavity occupancy of CO_2 molecules in small 5^{12} cavities are much higher than that in the large $5^{12}6^4$ cavities. Therefore, CO_2 was assumed to be only in small cavities. Based on further assumptions that CH_4 occupies both cavities while C_2H_6 and C_3H_8 only enter large $5^{12}6^4$ cavities of sII hydrates, the initial large-to-small cavity ratio of the mixed gas hydrate was around 0.9, which indicated that around 5/8 of the small cavities were empty. The ratio fluctuated and showed a sharp increase at the end of the

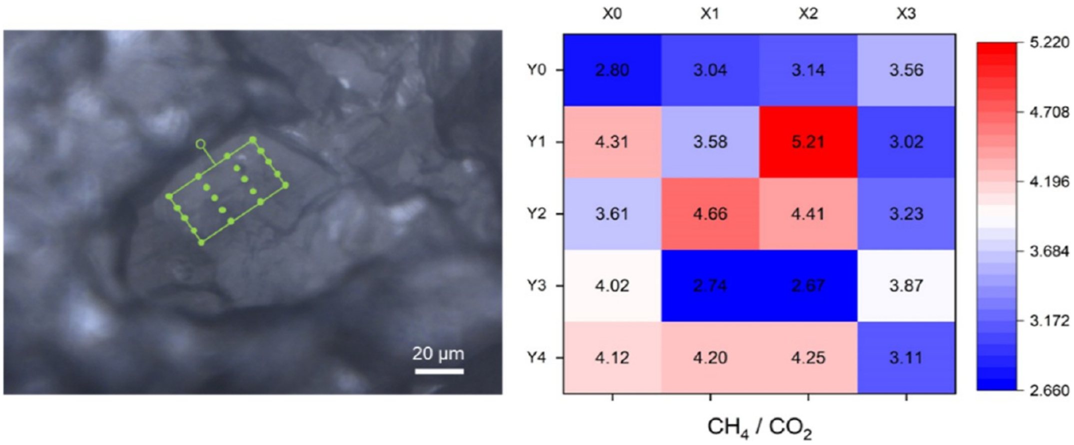

Figure 12. (a) Raman area mapping on a hydrate crystal surface with 4 × 5 defined points. (b) Variation in the CH_4/CO_2 concentration ratio recorded for the defined points.

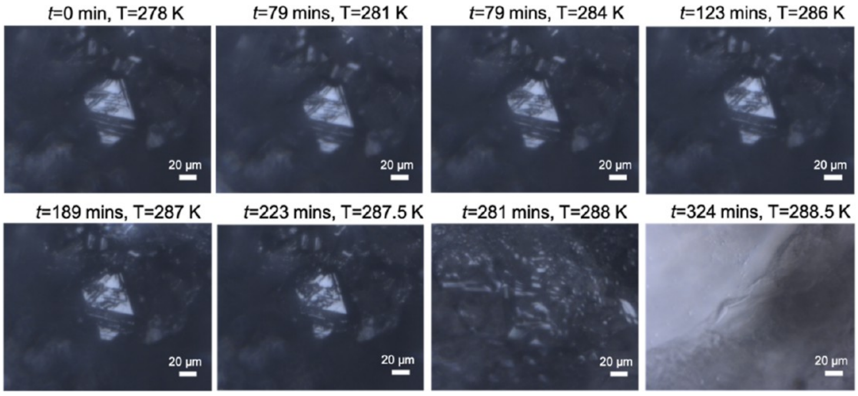

Figure 13. Surface morphological changes observed on one hydrate crystal at each specific temperature step during *in situ* Raman measurements.

dissociation process (Figure 17b). A similar trend was also observed when the experiment was repeated as shown in the Supporting Information Figure S3, despite the fact that the value of the large-to-small cavity ratio was different.

3.4. sII Multi-Component Mixed Hydrates—Molecular Dynamics Simulation.

The MD simulation results of the sII mixed gas hydrate dissociation were obtained under the same condition as that for the binary gas hydrates. Figure 18 shows the snapshots of the hydrate dissociation simulation on the (110) surface as well as the *z*-density profiles for all gas molecules. The layered dissociation of the hydrate, from the ends toward the middle, happened in the direction parallel to the hydrate interface. As previously mentioned, the early stage of the dissociation was promoted by collapsing the incomplete open cavities at the hydrate surface. After this rapid dissociation, the next hydrate layers became unstable and tended to collapse. The animation from the trajectories of the simulation is also given in the Supporting Information Animation S2.

As seen in Figure 18, the periodic peaks from z = ∼1.7 to ∼8.3 nm presenting the gas molecules encased in the hydrate cavities gradually disappeared from the two ends of the hydrate phase over time. By melting the hydrate crystals, a liquid and a gas phase formed so that the liquid phase was located between the hydrate and gas phases. The density of gas molecules at the liquid phase suddenly dropped, while that at the gas phase increased until the end. Therefore, the liquid phase region was located between two maxima in the density profile: a maximum of density at the hydrate phase surface (from the outermost hydrate layer) and another at the gas−liquid interface due to the excess gas density. It was previously observed that hydrocarbons and also CO_2 even with low concentrations preferentially adsorb at the gas−liquid surface, leading to an increase in the local density of the gases.[46]

Figure 19 shows the time evolution of the F_3 order parameter upon increasing the temperature of the system for different cross sections of the slab of mixed gas hydrate parallel to the z-direction. After around 13 ns, the dissociation of outermost layers 1 and 8 was started at a temperature of 284 K, and they completely collapsed, reaching the F_3 values of ∼0.07 at around 30 ns and 288 K. The temperature of 288 K was very close to the equilibrium temperature of the sII mixed gas hydrate and was also in agreement with that observed in the experimental part (Figure 13).

The rate of increasing the F_3 values of the inner layers of the hydrate was slowed down, and further dissociation was hindered due to recrystallization of some hydrate cavities around gas molecules diffusing in the liquid phase, as previously discussed. Figure 20 shows some snapshots of the mixed gas hydrate simulation to illustrate the recrystallization of hydrate cavities during the dissociation process. These partial cavities were usually formed in the vicinity of the hydrate surface due to the high concentration of the gas molecules in this region. However, after about 90 ns, the first inner layers 2 and 7 started melting at a temperature of 308 K, and finally, at 323 K, the F_3 values of the last inner hydrate

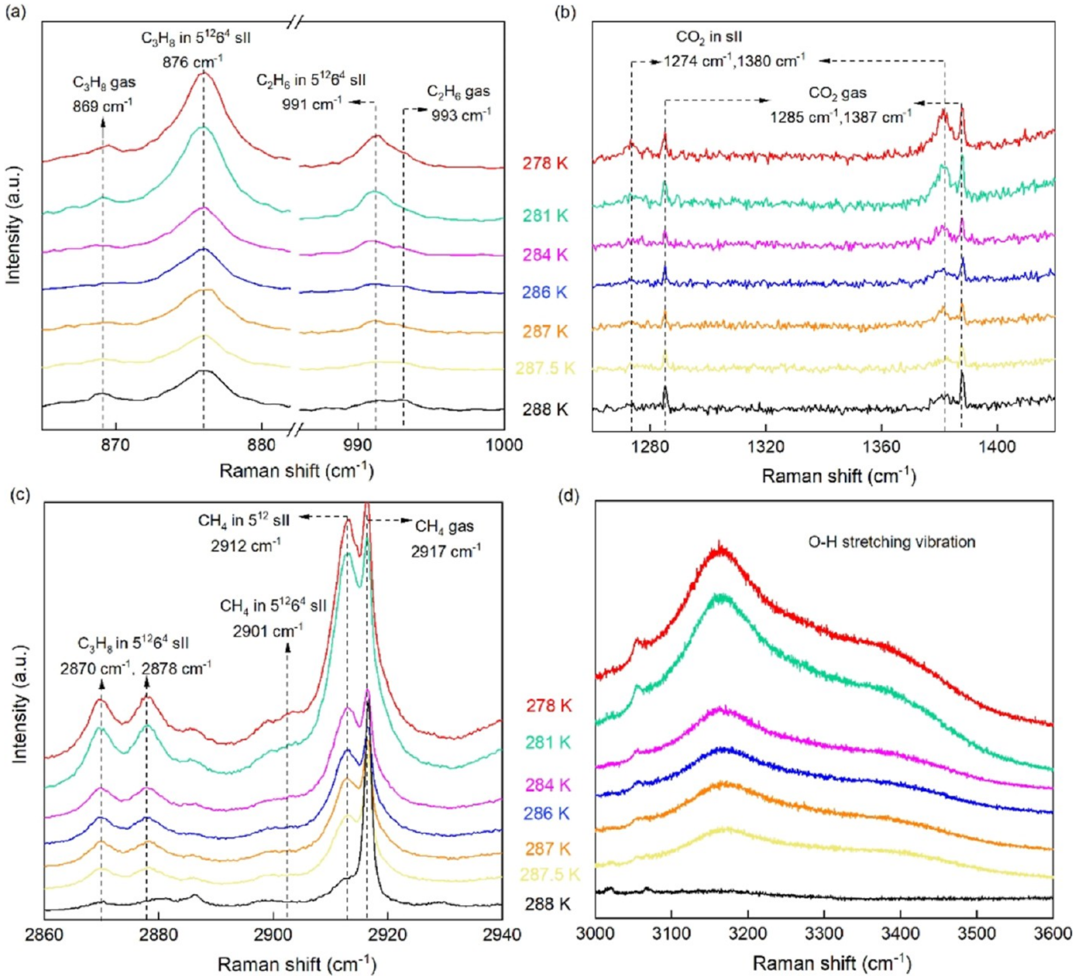

Figure 14. *In situ* Raman spectra of sII mixed gas hydrates at different temperature steps. (a) C−C stretching vibrational region; (b) C−O symmetric stretching and overtone bending for CO_2 molecules; (c) C−H stretching vibrational modes; (d) O−H stretching modes.

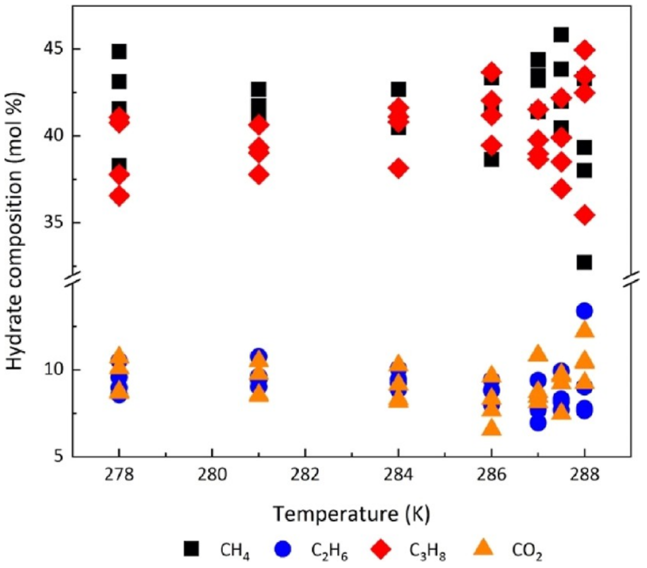

Figure 15. Changes in the composition of the hydrate phase with increasing temperatures calculated from *in situ* Raman spectroscopic measurements.

layers changed rapidly and approached a constant value of ∼0.08 after approximately 210 ns.

The time variation of the large-to-small cavity occupancy ratio remaining in the hydrate phase as well as the hydrate conversion are displayed in Figure 21. Although no major fluctuations were observed, there were slight variations in the large-to-small cavity occupancy ratio, and we tried to specify the reasonable trends for this parameter corresponding to the results from Figure 19. At the initial stage of the process, before dissociation of the first layers, the hydrate conversion remained constant at this period and the occupancy ratio decreased from a value of about 0.6, which was consistent with the 8:13 large-to-small cavity occupancy ratio designed for the unit cell (Table 1). This corresponded to the dissociation of the incomplete open cavities at two interfaces. After around 13 ns, the hydrate conversion decreased suddenly and a slight increase in the large-to-small cavity occupancy ratio was observed. It corresponded to the decomposition of two outermost layers between around 13 and 33 ns, implying that the small 5^{12} cavities were decomposed faster than the large $5^{12}6^4$ cavities (marked as stage A). Afterwards, the hydrate conversion showed no significant change until ∼90 ns; however, some slight fluctuations could be seen in the large-to-small cavity occupancy ratio, but they seemed to stagnate at around 0.65 during the period. This reflected a delayed dissociation process of the inner hydrate layers (as seen in Figure 19). After this time, the first inner layers started to dissociate, the hydrate conversion decreased, and the large-to-

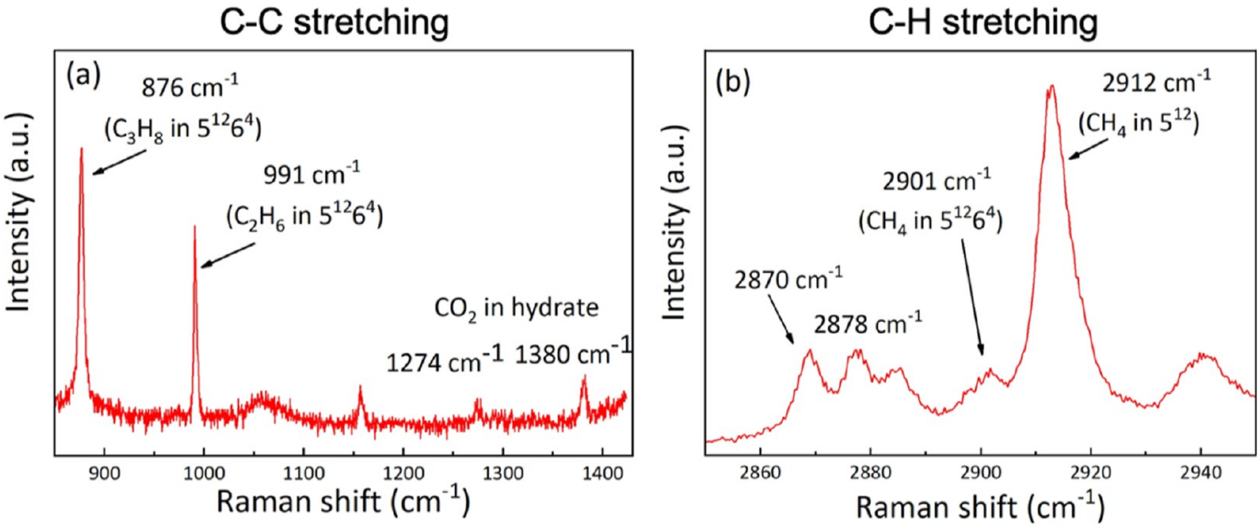

Figure 16. Raman spectra of the mixed hydrate phase observed from *ex situ* measurements showing (a) C−C stretching vibrations in the interval from 850 cm^{-1} to 1400 cm^{-1} and (b) C−H stretching vibrations from 2850 cm^{-1} to 2950 cm^{-1}.

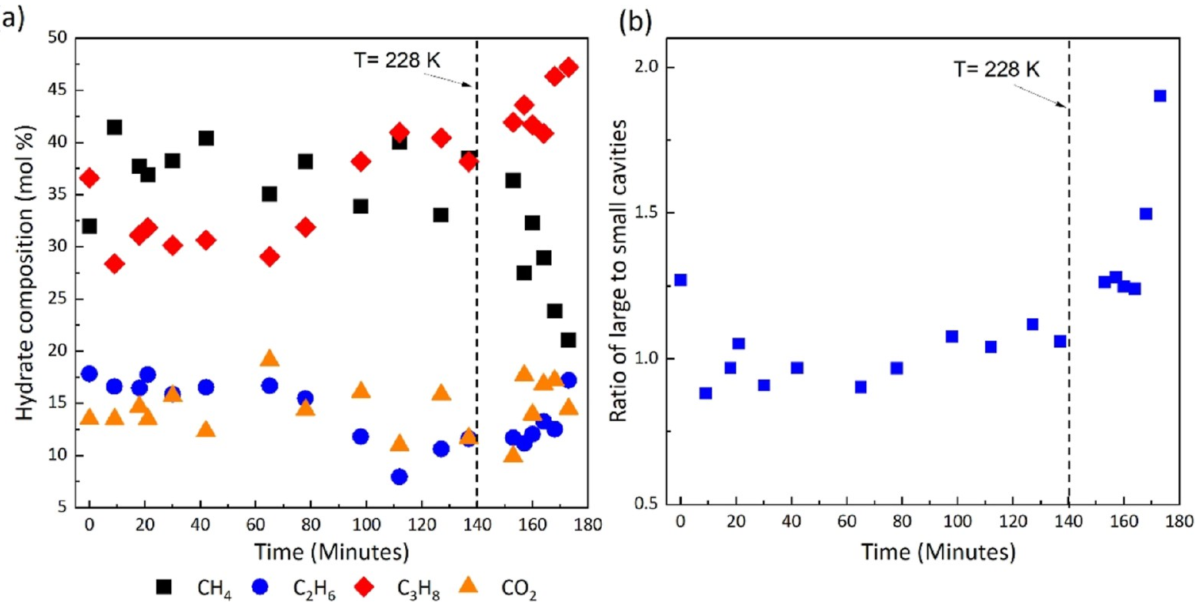

Figure 17. (a) Changes of composition in the hydrate phase. (b) Large-to-small cavity ratio of the multicomponent gas hydrates obtained from *ex situ* Raman measurements. The black dashed lines indicate the start of dissociation at T = 228 K after 140 mins.

small cavity occupancy ratio again increased for a time as long as 95 ns (marked as stage B). After ∼185 ns and close to the end of dissociation process, the data scattered, and therefore, there were no further evaluations.

From the experimental results for sII mixed gas hydrates, it was known that the large-to-small cavity occupancy ratio increased during the decomposition of sII hydrates, especially at the end, as seen in Figure 17b. This corresponds to the dissociation of the hydrate layers from the MD simulation results. So, the two stages of A and B, as defined in Figure 21, could be selected as the rate-controlling stages in the hydrate breakup of the sII mixed gas hydrate.

The composition of gas molecules in the hydrate phase during the dissociation process of the sII mixed gas hydrate is shown in Figure 22. The CH_4 concentration generally decreased at the beginning and at the end (>150 ns) of the hydrate breakup, while the relative proportion of C_3H_8 in the hydrate phase increased at that time; however, the data scattered pretty much. Since the compositions of two other gas molecules were very low, an interpretation of their proportion changes in the hydrate phase during the process was difficult. Nevertheless, an increase in the concentration of C_2H_6 and CO_2 molecules was observed at the end. This indicated that the cavities occupied with the CH_4 molecules were preferentially collapsed and a larger amount of CH_4 molecules compared to the others were released. These results were nearly in agreement with those reported in Figures 15 and 16a from the experimental measurements; however, the composition of these complex mixed hydrate crystals exhibited fluctuations over the process.

3.5. Hydrate Dissociation Kinetics and Mechanisms.

From Part I (ef-2022-03984u), it was experimentally found that the CH_4 molecules tend to escape from the large cavities ($5^{12}6^2$) faster than those in small cavities (5^{12}) during the

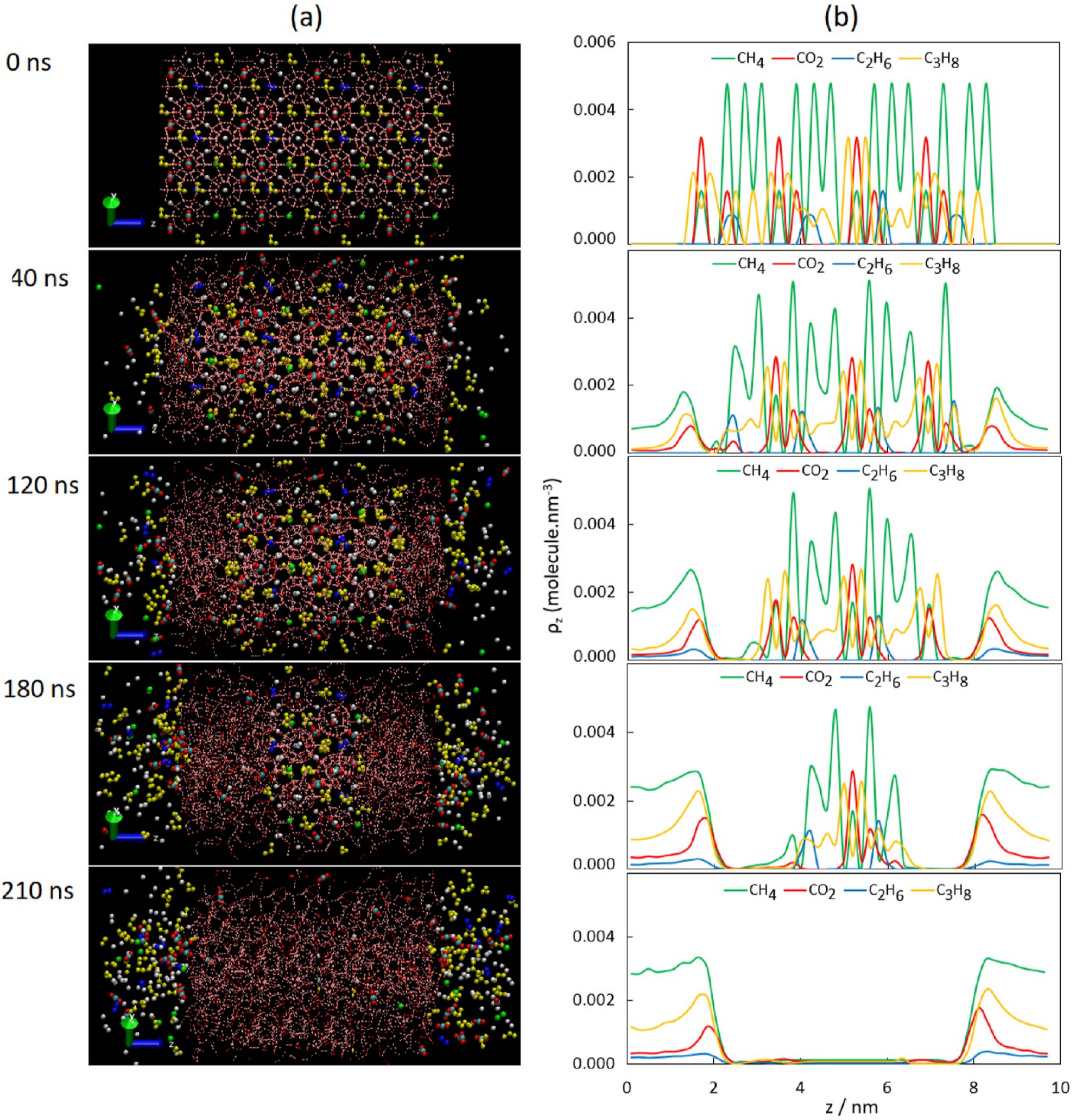

Figure 18. (a) Snapshots of sII mixed gas hydrate dissociation on the (110) surface at different times in the simulation trajectory. The hydrogen bonding in the hydrate phase is shown in red. CH_4 in the small cavity, CH_4 in the large cavity, and CO_2, C_2H_6, and C_3H_8 molecules are represented by white, green, cyan-red, blue, and yellow spheres, respectively. Each occupied hydrate cavity contains a maximum of one gas molecule. (b) The *z*-Density profile for the gas molecules during the dissociation process.

dissociation of sI CH_4 hydrates. It indicated that CH_4 molecules were expected to better stabilize in the small 5^{12} cavities than in the large $5^{12}6^2$ cavities. The same phenomenon was observed via MD simulation when the inner layers of the hydrate slab was dissociating. However, if the large cavities ($5^{12}6^4$) in the sII hydrate contain larger hydrocarbons such as C_2H_6 and C_3H_8, these cavities seem to be better stabilized than the small 5^{12} cavities filled with CH_4. For the CH_4−C_3H_8 hydrates, the molecular size of C_3H_8 was too big to fit into the small 5^{12} cavities.[47] In the sII mixed gas hydrates, CH_4 and CO_2 predominantly occupied small 5^{12} cavities and a small proportion of CH_4 was encased into the large $5^{12}6^4$ cavities together with C_2H_6 and C_3H_8. Both of the binary and mixed gas hydrates showed oscillations in the large-to-small cavity occupancy ratio at the beginning but an increase upon dissociation, implying that the gas molecules such as C_2H_6, C_3H_8 seem to better stabilize in the large $5^{12}6^4$ cavities than the small 5^{12} cavities stabilized by CH_4 and CO_2. Additionally, a preferential dissociation of CH_4 was confirmed from both experimental and numerical simulations.

Our results regarding the differentiated behavior of different guest molecules in hydrate cavities are in good agreement with the data reported by Truong-Lam et al.,[12] who also investigated the dissociation of binary CH_4/C_3H_8 mixed gas hydrates but with a varied composition by depressurization. The retention of C_3H_8 in the large $5^{12}6^4$ hydrate cavities during

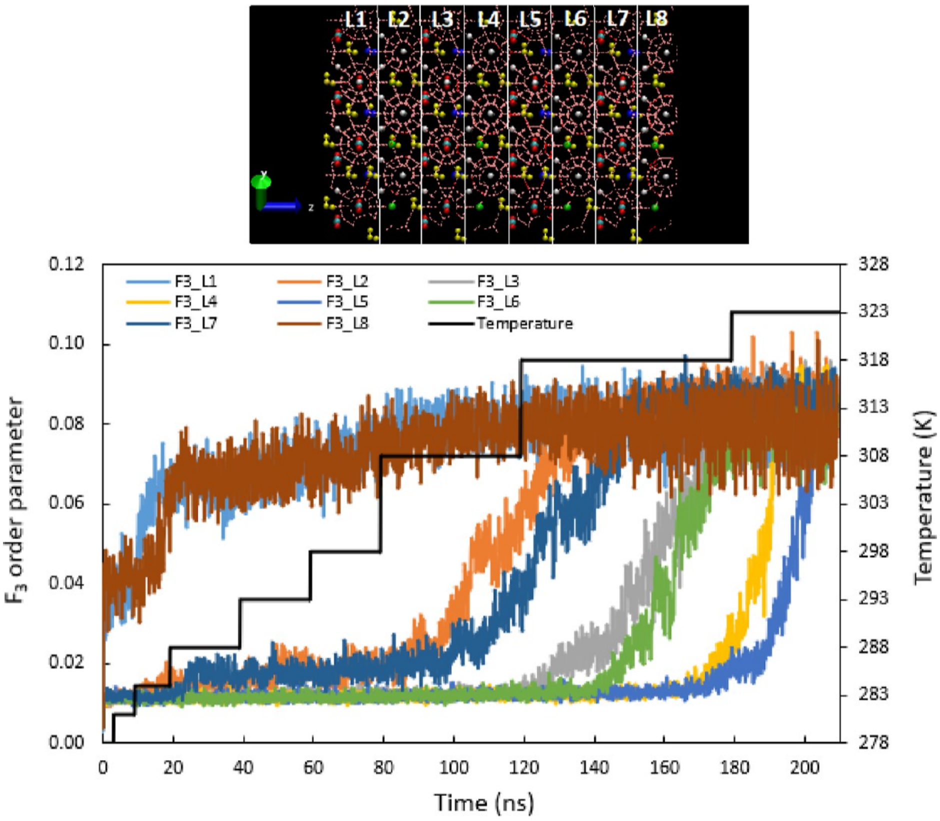

Figure 19. F_3 order parameter for the layered mixed gas hydrate slab along the z-direction. As shown, the hydrate phase was divided into eight layers, each with a thickness of around 0.875 nm and layers 1 and 8 forming the outermost layers with incomplete cavities.

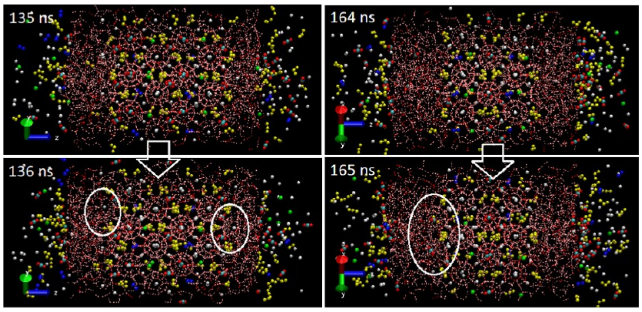

Figure 20. Snapshots of the mixed hydrate simulation on the (110) surface showing the recrystallization of hydrate cavities during the dissociation process. White circles show the recrystallized hydrate cavities.

dissociation was also inferred by Sun et al.[48] as a permeable barrier that restrained the diffusion of gas from the inner hydrate layers.

Notably, *ex situ* Raman measurements on both sI and sII hydrates indicated an early start of dissociation within the calculated stability field of hydrates. However, this is not the case for *in situ* Raman measurements. Hydrate samples for *ex situ* Raman measurements were synthesized from fine-grained ice powders, whereas deionized water was used in the *in situ* experiments. Since the simulation results indicated a layered dissociation of gas hydrates from the outermost layers to the inner ones, reactions are likely to take place via the surface/grain boundaries of gas hydrate crystals, in which grain size plays an important role. The grain size of the natural gas hydrate samples are in the range of 300−600 μm, while laboratory-formed hydrates are smaller by an order of magnitude as determined by high-energy synchrotron radiation.[49] As can be seen from Figures 5 and 13, the euhedral crystals formed from water in *in situ* measurements have a size ranging from 50 to 90 μm. Previous research from our lab applying the same procedure for the formation of ice powder has confirmed by means of scanning electron microscopy that the diameters of the ice particles were estimated to be around 10−20 μm.[50] Thus, hydrates formed from ice powder in the lab may have a smaller grain size as compared to natural samples or those synthesized from water. Hydrate crystals with smaller grain sizes have a larger surface area and may adjust easily to the temperature increase, thus leading to a faster dissociation at lower temperature conditions as compared to the bulk hydrates. In addition, the gas hydrates

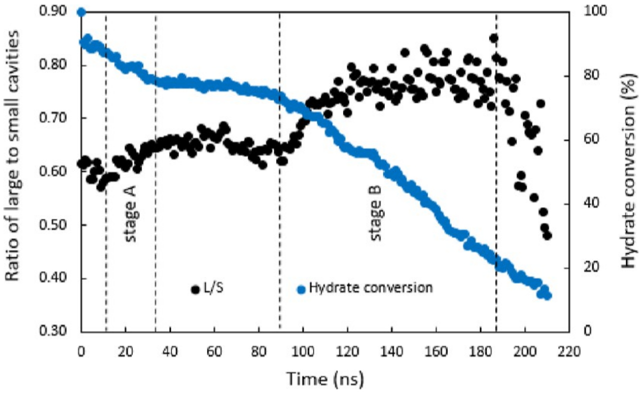

Figure 21. Ratio of large-to-small cavities and the hydrate conversion versus time for the sII mixed gas hydrate dissociation at 3.0 MPa and 278−323 K.

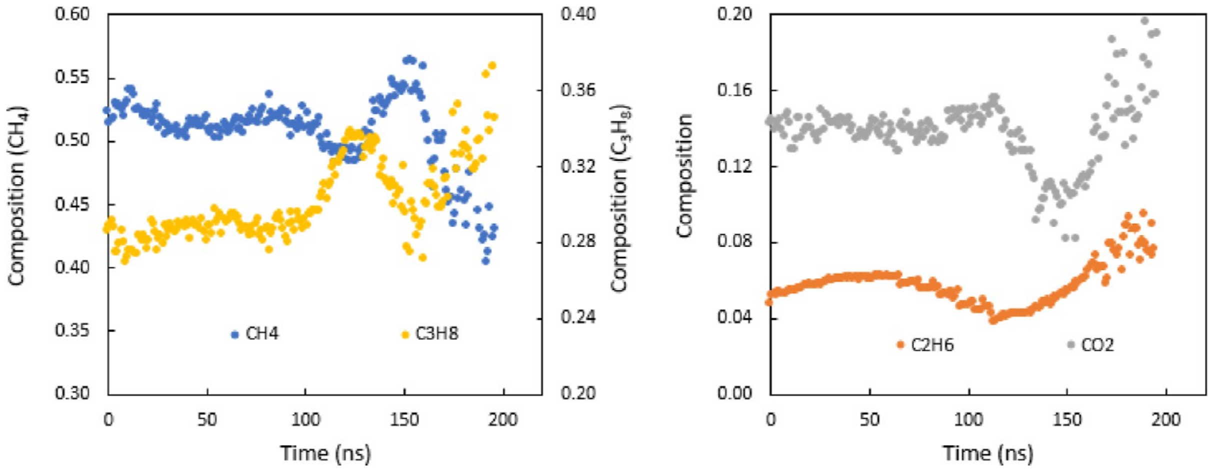

Figure 22. Composition of gas molecules in the hydrate phase versus time for the sII mixed gas hydrate dissociation.

formed in the laboratory may only reach a steady state but not the equilibrium condition with respect to composition and absolute cage occupancy. The calculation from CSMGem software is based on the model at an equilibrium state. For instance, CSMGem calculates a cavity occupancy of 85% of the small 5^{12} cavities and almost 100% of large $5^{12}6^4$ cavities for the binary gas hydrates (Table 1). However, based on the experimental data provided by *ex situ* Raman measurements, only 63% of the small 5^{12} cavities were occupied, which may result in a less stabilized hydrate phase and thus a shift in the dissociation temperature.

Besides the dissociation temperature, differences were also observed for hydrate composition and cavity occupancy from *in situ* and *ex situ* Raman measurements due to the varied experimental conditions. Hydrates were formed from an aqueous phase and a continuous gas flow in the *in situ* experiments, whereas the batch vessels were only pressurized once at the beginning of the hydrate formation for the *ex situ* measurements. The different hydrate formation conditions resulted in a slightly varied hydrate composition as compared to that in *in situ* experiments and modeling. However, the trends of the hydrate composition and cavity occupancy were generally consistent from *in situ* experiments, *ex situ* experiments, as well as numerical simulations, which supported a reliable and precise investigation of the hydrate dissociation behavior on a micrometer scale.

4. CONCLUSIONS

In this study, we presented our experimental and modeling investigations on the sII binary $CH_4-C_3H_8$ hydrates and sII multicomponent mixed gas hydrates during the dissociation process in response to thermal stimulation. Results obtained from the MD simulations qualitatively agreed with those from *in situ* and *ex situ* Raman spectroscopy, improving the understanding of the dissociation behavior of sII hydrates. The following points summarize the key findings and conclusions.

1. The results of two sII hydrate systems and sI CH_4 hydrate from Part I (ef-2022-03984u) confirmed that the dissociation behavior of the hydrates was affected by the structure and cavity occupancy of guest molecules in the hydrate phase.
2. Intrinsic kinetics (decomposition of the hydrate cavities consistent with the ratio of large-to-small cavities in the hydrate cell) may control the early stage of sII hydrate dissociation. Further dissociation was hindered because of the formation of a liquid phase as a result of the hydrate breakup. Unstable (partial) hydrate cavities could form within the liquid phase which was oversaturated with the gas molecules in the vicinity of the hydrate surface. Therefore, hydrates underwent a decomposition−reformation process until the decomposition was restarted.
3. There is preferential dissociation of hydrate cavities with different guests. The cavities occupied with CH_4 molecules preferentially collapsed and a larger amount of CH_4 was released compared to C_3H_8 molecules, leading to changes in the hydrate composition and an increase in the large-to-small cavity ratio during the dissociation of the binary sII hydrate. In the case of mixed hydrates, a relative increase of the C_3H_8, C_2H_6, and CO_2 concentration and an increase of the large-to-small cavity ratio in the hydrate phase were observed at the end of the dissociation process, implying that CH_4 and CO_2 in small cavities were released faster while C_2H_6 and C_3H_8 seemed to better stabilize in the large $5^{12}6^4$ cavities. This indicates the dependence of the dissociation behavior of the cavities on the properties of the specific guest molecule, especially the ability of the molecule to stabilize the cage.

This work showed that the integration of Raman spectroscopic measurements and molecular dynamics simulations made a better estimation of the dissociation behavior of gas hydrates with different structures and compositions. The investigation of the dissociation process of sII mixed gas hydrates, which frequently occur in natural reservoirs, may also be critically useful in the assessment of CH_4 release to the atmosphere from destabilization hydrate reservoirs in response to climate changes.

■ ASSOCIATED CONTENT

Data Availability Statement

Research data associated with this article can be accessed through GFZ data services. Pan, Mengdi; Schicks, Judith M. (2022): Raman spectroscopic data from dissociation behavior of sI CH_4 hydrates, sII $CH_4-C_3H_8$ hydrates and multicomponent mixed gas hydrates in terms of thermal stimulation. GFZ Data Services. https://doi.org/10.5880/GFZ.3.1.2022.

008. Naeiji, Parisa; Schicks, Judith M. (2022): Molecular dynamics simulation data for dissociation of CH_4 and mixed gas hydrates. GFZ Data Services. https://doi.org/10.5880/GFZ.3.1.2022.007.

Supporting Information

The Supporting Information is available free of charge at https://pubs.acs.org/doi/10.1021/acs.energyfuels.2c03985.

Animation from the simulation trajectory of sII CH_4+C_3H_8 hydrates (MPG)

Animation from the simulaton trajectory of sII mixed gas hydrates (MPG)

Raman spectroscopic data from repeated test and the temperature profile during the simulation trajectory of gas hydrates (PDF)

AUTHOR INFORMATION

Corresponding Author

Mengdi Pan – *GFZ German Research Centre for Geosciences, 14473 Potsdam, Germany; Key Laboratory of Gas Hydrate, Guangzhou Institute of Energy Conversion, Chinese Academy of Sciences, Guangzhou 510640, China; School of Chemical and Bioprocess Engineering, University College Dublin, Dublin 4, Ireland;* orcid.org/0000-0003-0632-1799; Email: mengdi.pan@ucd.ie

Authors

Parisa Naeiji – *GFZ German Research Centre for Geosciences, 14473 Potsdam, Germany;* orcid.org/0000-0003-2206-5510

Judith M. Schicks – *GFZ German Research Centre for Geosciences, 14473 Potsdam, Germany;* orcid.org/0000-0003-1106-0693

Complete contact information is available at: https://pubs.acs.org/10.1021/acs.energyfuels.2c03985

Author Contributions

∞M.P. and P.N. contributed equally to this paper. M.P.: Conceptualization, Experimental investigation, Writing—original draft, visualization; P.N.: Conceptualization, Numerical modeling investigation, Writing—original draft, Visualization; J.S.: Conceptualization, Writing—review & editing, Supervision.

Notes

The authors declare no competing financial interest.

ACKNOWLEDGMENTS

The authors sincerely acknowledge Dr. Erik Spangenberg and Ronny Giese for their invaluable technical support during the experiments. M.P. would like to appreciate the financial support from the Chinese Scholarship Council (no. 201704910817) and the Open Fund Project of the Key Laboratory of Natural Gas Hydrate, Chinese Academy of Sciences (E129kf1401).

REFERENCES

(1) von Stackelberg, M.; Müller, H. R. Zur Struktur Der Gashzdrate. *Naturwissenschaften* **1951**, *38*, 456.

(2) Stackelberg, M. Feste Gashydrate. *Naturwissenschaften* **1949**, *36*, 327–333.

(3) Lu, H.; Seo, Y.; Lee, J.; Moudrakovski, I.; Ripmeester, J. A.; Chapman, N. R.; Coffin, R. B.; Gardner, G.; Pohlman, J. Complex Gas Hydrate from the Cascadia Margin. *Nature* **2007**, *445*, 303–306.

(4) Sloan, E. D.; Koh, C. A. *Clathrate Hydrates of Natural Gases*, 3rd ed.; CRC Press Taylor and Francis Group: Boca Raton, FL, USA, 2008.

(5) Subramanian, S.; Kini, R. A.; Dec, S. F.; Sloan, E. D. Evidence of Structure II Hydrate Formation from Methane plus Ethane Mixtures. *Chem. Eng. Sci.* **2000**, *55*, 1981–1999.

(6) Ripmeester, J. A.; Tse, J. S.; Ratcliffe, C. I.; Powell, B. M. A New Clathrate Hydrate Structure. *Nature* **1987**, *325*, 135–136.

(7) Naeiji, P.; Pan, M.; Luzi-Helbing, M.; Alavi, S.; Schicks, J. M. Experimental and Simulation Study for the Dissociation Behavior of Gas Hydrates – Part I: CH_4 Hydrates. *Energy Fuels* **2023**, DOI: 10.1021/acs.energyfuels.2c03984.

(8) Luzi-Helbing, M.; Naumann, R.; Girod, M.; Schicks, J. M. *Dissociation Kinetics of CH4 Hydrate, Mixed CH4+CO2 Hydrate and Mixed SII Hydrates.* In *Proceedings of the 9th International Conference on Gas Hydrates*; : Denver, USA, 2017.

(9) Tang, C.; Zhou, X.; Li, D.; Zhao, X.; Liang, D. In Situ Raman Investigation on Mixed CH4 -C3H8 Hydrate Dissociation in the Presence of Polyvinylpyrrolidone. *Fuel* **2018**, *214*, 505–511.

(10) Gupta, A.; Dec, S. F.; Koh, C. A.; Sloan, E. D. NMR Investigation of Methane Hydrate Dissociation. *J. Phys. Chem. C* **2007**, *111*, 2341–2346.

(11) Zhou, X.; Long, Z.; Liang, S.; He, Y.; Yi, L.; Li, D.; Liang, D. In Situ Raman Analysis on the Dissociation Behavior of Mixed CH4-CO2 Hydrates. *Energy and Fuels* **2016**, *30*, 1279–1286.

(12) Truong-Lam, H. S.; Seo, S. D.; Kim, S.; Seo, Y.; Lee, J. D. In Situ Raman Study of the Formation and Dissociation Kinetics of Methane and Methane/Propane Hydrates. *Energy and Fuels* **2020**, *34*, 6288–6297.

(13) Ding, L. Y.; Geng, C. Y.; Zhao, Y. H.; Wen, H. Molecular Dynamics Simulation on the Dissociation Process of Methane Hydrates. *Mol. Simul.* **2007**, *33*, 1005–1016.

(14) English, N. J.; Johnson, J. K.; Taylor, C. E. Molecular-Dynamics Simulations of Methane Hydrate Dissociation. *J. Chem. Phys.* **2005**, *123*, 244503.

(15) Iwai, Y.; Nakamura, H.; Arai, Y.; Shimoyama, Y. Analysis of Dissociation Process for Gas Hydrates by Molecular Dynamics Simulation. *Mol. Simul.* **2010**, *36*, 246–253.

(16) Sun, Z.; Wang, H.; Yao, J.; Yang, C.; Kou, J.; Bongole, K.; Xin, Y.; Li, W.; Zhu, X. Different Mechanism Effect between Gas-Solid and Liquid-Solid Interface on the Three-Phase Coexistence Hydrate System Dissociation in Seawater: A Molecular Dynamics Simulation Study. *Energies* **2018**, *11*, 6.

(17) Myshakin, E. M.; Jiang, H.; Warzinski, R. P.; Jordan, K. D. Molecular Dynamics Simulations of Methane Hydrate Decomposition. *J. Phys. Chem. A* **2009**, *113*, 1913–1921.

(18) Kondori, J. *Modeling Investigation of Gas Hydrate Decomposition: Thermodynamic Approach and Molecular Dynamic Simulations*; Memorial University of Newfoundland, 2019.

(19) Schicks, J. M.; Pan, M.; Giese, R.; Poser, M.; Ismail, N. I.; Luzi-Helbing, M.; Bleisteiner, B.; Lenz, C. A New High-Pressure Cell for Systematic in Situ Investigations of Micro-Scale Processes in Gas Hydrates Using Confocal Micro-Raman Spectroscopy. *Rev. Sci. Instrum.* **2020**, *91*, 115103.

(20) Pan, M.; Schicks, J. M. *Raman Spectroscopic Data from Dissociation Behavior of SI CH4 Hydrates, SII CH4-C3h8 Hydrates and Multicomponent Mixed Gas Hydrates in Terms of Thermal Stimulation*; GFZ Data Services, 2022.

(21) Van Der Spoel, D.; Lindahl, E.; Hess, B.; Groenhof, G.; Mark, A. E.; Berendsen, H. J. GROMACS: Fast, Flexible, and Free. *J. Comput. Chem.* **2005**, *26*, 1701–18.

(22) Takeuchi, F.; Hiratsuka, M.; Ohmura, R.; Alavi, S.; Sum, A. K.; Yasuoka, K. Water Proton Configurations in Structures I, II, and H Clathrate Hydrate Unit Cells. *J. Chem. Phys.* **2013**, *138*, 124504.

(23) Abascal, J. L. F.; Sanz, E.; García Fernández, R. G.; Vega, C. A Potential Model for the Study of Ices and Amorphous Water: TIP4P/Ice. *J. Chem. Phys.* **2005**, *122*, 234511.

(24) Eggimann, B. L.; Sunnarborg, A. J.; Stern, H. D.; Bliss, A. P.; Siepmann, J. I. An Online Parameter and Property Database for the TraPPE Force Field. *Mol. Simul.* **2014**, *40*, 101−105.

(25) Martin, M. G.; Siepmann, J. I. Transferable Potentials for Phase Equilibria. 1. United-Atom Description of n-Alkanes. *J. Phys. Chem. B* **1998**, *102*, 2569−2577.

(26) Hess, B.; Bekker, H.; Berendsen, H. J. C.; Fraaije, J. G. E. M. LINCS: A Linear Constraint Solver for Molecular Simulations. *J. Comput. Chem.* **1997**, *18*, 1463−1472.

(27) Docherty, H.; Galindo, A.; Vega, C.; Sanz, E. A Potential Model for Methane in Water Describing Correctly the Solubility of the Gas and the Properties of the Methane Hydrate. *J. Chem. Phys.* **2006**, *125*, 074510.

(28) Alavi, S.. *Molecular Simulations: Fundamentals and Practice*; Wiley-VCH Verlag GmbH: Weinheim, Germany, 2020; Vol. *1*.

(29) Darden, T.; York, D.; Pedersen, L. Particle Mesh Ewald: An N·log(N) Method for Ewald Sums in Large Systems. *J. Chem. Phys.* **1993**, *98*, 10089−10092.

(30) Berendsen, H. J. C.; Postma, J. P. M.; van Gunsteren, W. F.; DiNola, A.; Haak, J. R. Molecular Dynamics with Coupling to an External Bath. *J. Chem. Phys.* **1984**, *81*, 3684−3690.

(31) Hockney, R. W.; Goel, S. P.; Eastwood, J. W. Quiet High-Resolution Computer Models of a Plasma. *J. Comput. Phys.* **1974**, *14*, 148−158.

(32) BÂEZ, L. A.; CLANCY, P. Computer Simulation of the Crystal Growth and Dissolution of Natural Gas Hydrates. *Ann. N.Y. Acad. Sci.* **1994**, *715*, 177−186.

(33) Naeiji, P.; Schicks, J. M. *Molecular Dynamics Simulation Data for Dissociation of CH4 and Mixed Gas Hydrates*; GFZ Data Services, 2022.

(34) Jeffrey, G. A. Hydrate Inclusion Compounds. *J. Incl. Phenom.* **1984**, *1*, 211−222.

(35) Burke, E. A. J. Raman Microspectrometry of Fluid Inclusions. *Lithos* **2001**, *55*, 139−158.

(36) Schrader, B. *Infrared and Raman Spectroscopy: Methods and Applications*; VCH Verlagsgesellschaft mbH: Weinheim, Germany, 1995.

(37) Naeiji, P.; Woo, T. K.; Alavi, S.; Varaminian, F.; Ohmura, R. Interfacial Properties of Hydrocarbon/Water Systems Predicted by Molecular Dynamic Simulations. *J. Chem. Phys.* **2019**, *150*, 114703.

(38) Alavi, S.; Ripmeester, J. A. Nonequilibrium Adiabatic Molecular Dynamics Simulations of Methane Clathrate Hydrate Decomposition. *J. Chem. Phys.* **2010**, *132*, 144703.

(39) Vatamanu, J.; Kusalik, P. G. Molecular Insights into the Heterogeneous Crystal Growth of SImethane Hydrate. *J. Phys. Chem. B* **2006**, *110*, 15896−15904.

(40) Choudhary, N.; Chakrabarty, S.; Roy, S.; Kumar, R. A Comparison of Different Water Models for Melting Point Calculation of Methane Hydrate Using Molecular Dynamics Simulations. *Chem. Phys.* **2019**, *516*, 6−14.

(41) Chen, L.; Lu, H.; Ripmeester, J. A. Raman Spectroscopic Study of CO2 in Hydrate Cages. *Chem. Eng. Sci.* **2015**, *138*, 706−711.

(42) Schicks, J. M.; Luzi-Helbing, M. Cage Occupancy and Structural Changes during Hydrate Formation from Initial Stages to Resulting Hydrate Phase. *Spectrochim. Acta Part A Mol. Biomol. Spectrosc.* **2013**, *115*, 528−536.

(43) Uchida, T.; Takeya, S.; Kamata, Y.; Ohmura, R.; Narita, H. Spectroscopic Measurements on Binary , Ternary , and Quaternary Mixed-Gas Molecules in Clathrate Structures. *Ind. Eng. Chem. Res.* **2007**, *46*, 5080−5087.

(44) Sum, A. K.; Burruss, R. C.; Sloan, E. D. Measurement of Clathrate Hydrates via Raman Spectroscopy. *J. Phys. Chem. B* **1997**, *101*, 7371−7377.

(45) Walrafen, G. E.; Yang, W. H.; Chu, Y. C. Raman Evidence for the Clathratelike Structure of Highly Supercooled Water. *ACS Symp. Ser.* **1997**, *676*, 287−308.

(46) Naeiji, P.; Woo, T. K.; Alavi, S.; Ohmura, R. Molecular Dynamics Simulations of Interfacial Properties of the CO2-Water and CO2-CH4-Water Systems. *J. Chem. Phys.* **2020**, *153*, 044701.

(47) Lederhos, J. P.; Christiansen, R. L.; Sloan, E. D. A First Order Method of Hydrate Equilibrium Estimation and Its Use with New Structures. *Fluid Phase Equilib.* **1993**, *83*, 445−454.

(48) Sun, Y. H.; Su, K.; Li, S. L.; Carroll, J. J.; Zhu, Y. H. Experimental Investigation into the Dissociation Behavior of CH4-C2H6-C3H8 Hydrates in Sandy Sediments by Depressurization. *Energy Fuels* **2018**, *32*, 204−213.

(49) Klapp, S. A.; Klein, H.; Kuhs, W. F. First Determination of Gas Hydrate Crystallite Size Distributions Using High-Energy Synchrotron Radiation. *Geophys. Res. Lett.* **2007**, *34*(). DOI: 10.1029/2006gl029134

(50) Luzi, M.; Schicks, J. M.; Naumann, R.; Erzinger, J. Systematic Kinetic Studies on Mixed Gas Hydrates by Raman Spectroscopy and Powder X-Ray Diffraction. *J. Chem. Thermodyn.* **2012**, *48*, 28−35.